Initial stages of nucleation in phase separating polymer blends

A. A. Lefebvre, J. H. Lee, H. S. Jeon, and N. P. Balsara[a)]
Department of Chemical Engineering, Chemistry, and Materials Science, Polytechnic University, Six Metrotech Center, Brooklyn, New York 11201

B. Hammouda
National Institute of Standards and Technology, Building 235, E 151, Gaithersburg, Maryland 20899

(Received 20 April 1999; accepted 6 July 1999)

The initial stages of nucleation during liquid–liquid phase separation in mixtures of high molecular weight polymers was studied by time-resolved small angle neutron scattering. Phase separation was induced either by decreasing temperature or by increasing pressure. One of the blend components was labeled with deuterium to obtain sufficient scattering contrast between the components. The general features of nucleation were independent of quench depth and the nature of the quench (temperature quench versus pressure quench). The early stages of nucleation consisted of amplification of concentration fluctuations. During this stage, the scattered intensity (I) in the low scattering vector (q) limit was consistent with the Ornstein–Zernike equation. This enabled the determination of the characteristic length scale of the growing fluctuations, ξ. The I vs q behavior at intermediate scattering vectors ($q>1/\xi$) could be described by a power law ($I\sim q^{-d}$). We demonstrate the existence of a time–temperature superposition principle during nucleation: The time dependence of d at different quench depths could be superimposed by a lateral shift of the data along the time axis (log scale). In analogy to the shift factor for viscoelastic behavior of polymers, we define a nucleation shift factor, a_N, which describes the slowing down of nucleation kinetics with decreasing quench depth. Similarly, nucleation after pressure quenches can be described by a time–pressure superposition law. For each quench, we find that the scattering intensity is independent of time in the high q regime ($q>q_{\text{merge}}$). This implies the absence of growing structures with length scales smaller than $\xi_{\text{crit}}=1/q_{\text{merge}}$ during nucleation. This aspect of nucleation is consistent with classical theories which predict the existence of a critical nucleus size. As expected, ξ_{crit} increases with decreasing quench depth.
[S0021-9606(99)50437-6]

I. INTRODUCTION

Phase separation in liquid mixtures can occur either by spinodal decomposition or nucleation.[1–3] The classical theory of spinodal decomposition indicates that phase separation is initiated by the amplification of selected Fourier modes of concentration fluctuations that preexist in the homogeneous liquid.[2] The signature of this process in scattering experiments is a scattering peak that brightens as phase separation proceeds. Remarkable agreement between theory and experiment has been reported in mixtures of ordinary liquids (with waterlike viscosity), metals, glasses, ceramics, and polymers.[2–17] In contrast, the signatures of the initial stage of nucleation are not well established. The classical theory of nucleation is based on the assumption that during the initial stages of the transformation, a few molecules rearrange themselves into droplets or nuclei that have all of the characteristics (composition, density, and symmetry) of the new phase.[1] In liquid–liquid phase separation, the composition difference is the main factor that differentiates the nuclei from the surrounding mother phase. If the radius of these nuclei exceeds a certain critical radius, then the growth of the new phase is spontaneous. Theoretical aspects of the evolution of such systems were studied by Langer and Schwartz[18] and others.[2] On the other hand, computer simulations of nucleation have revealed the formation and growth of clusters with varying shape and compactness.[19–22] Optical techniques have been used in experimental studies of nucleation in mixtures of low molecular weight compounds,[23] colloidal suspensions,[24] and polymer mixtures.[25] However, the initial stages of phase separation and the formation of the critical nucleus were not resolved in any of the experiments.[23–25]

The main purpose of this paper is to present experimental data obtained during the initial stages of nucleation. This was accomplished by conducting time-resolved neutron scattering experiments on mixtures of high molecular weight polymers. Molecular motion in melts of high molecular weight polymers is slow due to chain entanglement.[26] This expands the nucleation time scales and enables time-resolved measurements. Substantial scattering contrast between the components is required in order to obtain measurable signals from the subtle clustering processes that occur during the early stages of nucleation. This is accomplished by labeling one of the components in the mixture with deuterium. Classic experiments by Herkt-Maetzky and Schelten demonstrated that concentration fluctuations in homogeneous samples in the single-phase region could be studied by neu-

a)Author to whom correspondence should be addressed; electronic mail: nbalsara@duke.poly.edu

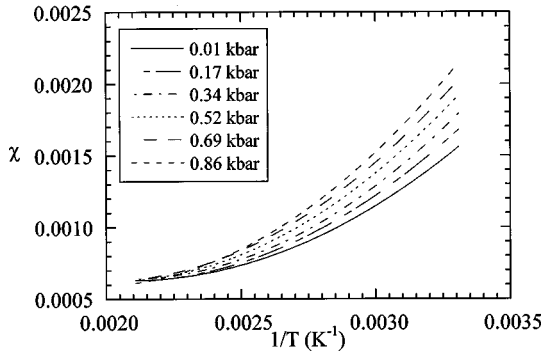

FIG. 1. The dependence of χ on temperature and pressure in PMB/PEB blends. This plot is based on data in Refs. 31 and 32.

tron scattering if one of the components is deuterated.[27] Therefore, clustering of chains during the initial stages of nucleation, which must necessarily lead to an increase in the scattering intensity, is, in principle, within detection limits.

In this study, we examine mixtures of hydrogenous and deuterated polyolefins. Since all polyolefins are saturated hydrocarbons (the empirical formula CH_2 applies to all members of the polyolefin family), the interactions between different components are expected to be nonspecific and dispersive in nature. The thermodynamic properties of a wide variety of polyolefin mixtures can be described by the Flory–Huggins model.[28–30] The Gibbs energy of mixing per unit volume for binary mixtures is given by

$$\frac{\Delta G}{kT}=\left[\frac{\phi \ln \phi}{v_A N_A}+\frac{(1-\phi)\ln(1-\phi)}{v_B N_B}\right]+\frac{\chi}{v_0}\phi(1-\phi), \quad (1)$$

where k is the Boltzmann constant, ϕ is the volume fraction of component A in the mixture, N_i is the number of monomers per chain of component i, v_i is the volume of each monomer of component i, χ is the Flory–Huggins interaction parameter, and v_0 is an arbitrary reference volume which we set equal to the mean monomer volume of the polymers chosen for this study at atmospheric conditions, 149 Å^3. The first two terms in Eq. (1) reflect the combinatorial entropy of mixing. We use the last term for all of the other contributions to ΔG, including changes in the internal energy and the volume change of mixing.[31] These effects are manifested in the temperature and pressure dependence of χ.

The particular polyolefins that we have used in this study are polymethylbutylene (PMB) and polyethylbutylene (PEB). The temperature and pressure dependence of the χ parameter between PMB and PEB chains has been reported in previous publications[31–34] and the results are summarized in Fig. 1. The χ parameter (or equivalently, ΔG) can be increased by either decreasing temperature or by increasing pressure. Phase separation can thus be initiated by either a decrease in temperature or by an increase in pressure. In this paper, we study nucleation triggered by both temperature and pressure quenches.

Our studies on polyolefin blends are also motivated by their technological importance. The current annual production of polyolefins (5×10^{10} kg/yr) exceeds that of any other man-made solid material. Most commercial polyolefins are used as blends. In some cases, the blending is done on purpose, to impart particular properties to the material. In other cases, blends are produced inadvertently, due to uncontrolled side reactions. Understanding the properties of polyolefin blends is also relevant to problems related to recycling polymeric waste, which is dominated by polyolefinic components.

This paper is part of a series on the thermodynamics of polyolefin blends.[17,31–42] In earlier work, we studied binary and multicomponent polyolefin mixtures using neutron scattering. We compared our experimental data with theoretical predictions based on the random phase approximation (RPA).[31–34] We demonstrated that the measured scattering profiles were in quantitative agreement with multicomponent RPA predictions without any adjustable parameters. We also examined the early stages of liquid–liquid phase separation by spinodal decomposition in polyolefin blends.[17] In this paper, we focus on nucleation in mixtures that are very similar to those studied in Refs. 17, 31–35, and 37. A preliminary report of our findings in the nucleation regime was published in Ref. 35.

II. EXPERIMENT

A. Materials

Nearly monodisperse model polyolefins were synthesized following the methodology of Rachapudy *et al.*[43] Homopolymers—polymethylbutylene and polyethylbutylene—were synthesized in two steps using isoprene and ethylbutadiene, respectively, as monomers. The polymerizations were conducted under high vacuum[44] in cyclohexane and the polydienes consisted of predominantly (93%) 1, 4 addition. Separate aliquots of the polydienes were then saturated in the presence of a palladium catalyst with H_2 and D_2 to yield fully hydrogenated and partially deuterated polyolefins. A pair of hydrogenous and partially deuterated polymethylbutylene-*block*-polyethylbutylene copolymers were synthesized by sequential anionic polymerization of isoprene and ethylbutadiene followed by saturation with H_2 and D_2. The polyolefins are essentially derivatives of polyethylene and are chemically equivalent to alternating ethylene–propylene and ethylene–butene copolymers. In this paper we refer to the poly(methylbutylene) chains as PMB and the poly(ethylbutylene) chains as PEB, where the letters *M* and *E* refer to the methyl and ethyl branches emanating from the C–C backbone. The chemical structures of the polymer chains used in this study are shown below.

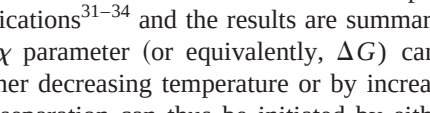

The characteristics of the polymers were determined using the procedures described in Ref. 33 and are listed in Table I. Polymers are named on the basis of composition. The prefix *h* refers to the hydrogenated polymers and the prefix *d* refers to partially deuterated polymers. Using methods discussed in Refs. 33 and 40, it was determined that the neutron scattering contrast between the blocks in *d*PMB–*d*PEB is negligible. The neutron scattering length

TABLE I. Characteristics of polymers.

Polymer	Density (g/cm^3)	No. of deuterium per six carbon atoms	Molecular weight (g/mol)	Polydispersity index	Volume fraction of PEB in block copolymer	Neutron scattering length density ($Å^{-2}$)
*h*PMB	0.8540	···	1.7×10^5	1.07	···	-3.04×10^{-7}
*d*PMB	0.9300	7.33	1.8×10^5	1.07	···	4.37×10^{-6}
*h*PEB	0.8628	···	2.2×10^5	1.08	···	-3.07×10^{-7}
*d*PEB	0.9272	6.15	2.4×10^5	1.08	···	3.65×10^{-6}
*h*PMB–*h*PEB	0.8562	···	2.0×10^5	1.10	0.33	-3.06×10^{-7}
*d*PMB–*d*PEB	0.9048	4.68	2.1×10^5	1.10	0.33	2.69×10^{-6}

density of each component was calculated using the methods described in Ref. 33 and is listed in Table I. The scattering contrast between the hydrogeneous components is negligible.

The experiments were performed on ternary blends of PMB, PEB, and PMB–PEB mixtures. The blends were made by dissolving the components in cyclohexane and then drying to a constant weight in a vacuum oven at 70 °C. The composition of the blends discussed in this paper are listed in Table II. The ratio of homopolymer volume fractions, ϕ_{PEB}/ϕ_{PMB}, was 0.34 in all of the blends (ϕ_i is the volume fraction of species i in the mixture, i=PEB, PMB, or PMB–PEB). The composition of each blend is thus determined by the volume fraction of the block copolymer, i.e., $\phi_{PMB-PEB}$. The blends are labeled Tx or Px where the letter T indicates that the blend was subjected to temperature quenches, while the letter P indicates that the blend was subjected to pressure quenches and x/100 is the volume fraction of the block copolymer in the blend. For example, the name T20, indicates that this blend was used in the temperature quench experiments and $\phi_{PMB-PEB}=0.2$. All of the blends contained one deuterated species. Since the scattering contrast between hydrogeneous components is negligible, the neutron scattering profiles are related to intramolecular and intermolecular correlations of the labeled species.

B. Small-angle neutron scattering

Small-angle neutron scattering (SANS) experiments were conducted on the NG3 beamline at the National Institute of Standards and Technology in Gaithersburg, MD. Two types of SANS experiments were performed on each sample. First, the limits of stability and metastability (the phase diagram) for each blend were estimated from static SANS experiments. Then time-resolved SANS measurements were taken to follow the kinetics of phase separation. The series of experiments reported in this paper were conducted during five separate sessions, each lasting three to four days.

TABLE II. Blend compositions.

Sample	Blend components	$\phi_{PMB-PEB}$	ϕ_{PMB}	ϕ_{PEB}	ϕ_{PEB}/ϕ_{PMB}
T20	*h*PMB–*h*PEB/*h*PMB/*d*PEB	0.204	0.594	0.202	0.340
T40	*h*PMB–*h*PEB/*h*PMB/*d*PEB	0.399	0.449	0.152	0.339
T50	*h*PMB–*h*PEB/*h*PMB/*d*PEB	0.501	0.373	0.126	0.338
T40D	*d*PMB–*d*PEB/*h*PMB/*h*PEB	0.407	0.444	0.149	0.336
T50′	*h*PMB–*h*PEB/*h*PMB/*d*PEB	0.499	0.375	0.125	0.333
P35	*h*PMB–*h*PEB/*d*PMB/*h*PEB	0.354	0.484	0.163	0.337

The phase diagram was determined using configuration A: neutron wavelength, $\lambda=6.0$ Å, wavelength spread, $\Delta\lambda/\lambda=0.15$, sample-to-detector distance=11 m, sample aperture=0.635 cm, source-to-sample distance=10.12 m, and source size=5.0 cm. The phase separation kinetics were followed using configuration B: neutron wavelength, $\lambda=14$ Å, wavelength spread, $\Delta\lambda/\lambda=0.15$, sample-to-detector distance=13.18 m, sample aperature=0.635 cm, source-to-sample distance=14.77 m, and source size=5.0 cm. Configuration B allowed access to scattering vectors, q, as low as 0.02 nm^{-1} [$q=4\pi\sin(\theta/2)/\lambda$, θ is the scattering angle].

The temperature quenches were conducted on 1-mm-thick samples held between quartz windows separated by an aluminum spacer. The apparatus used for the pressure quenches on sample P35 is described in Ref. 37. The sample was held in a thermostated steel pressure chamber between two sapphire windows separated by a 1.5 mm o ring. (After assembly the o ring is squeezed to a thickness of about 1 mm.) The o ring was surrounded by silicone oil, which served as the pressurizing fluid. A computer-driven piston assembly was used to control the sample pressure.

The scattering data were collected using a 128×128 pixel two-dimensional detector, corrected for background scattering, empty cell scattering, and detector sensitivity. All of the scattering profiles were azimuthally symmetric. We thus report the azimuthally averaged scattering intensity, I, as a function of q.

III. RESULTS AND DISCUSSION

A. Determination of phase diagrams

Typical static small-angle neutron scattering (SANS) profiles obtained from the T-series blends are shown in Fig. 2(a), where we show the intensity, I, vs q obtained from the T20 blend as a function of temperature. A substantial increase in the low-q scattering is evident as the temperature is decreased. Qualitatively similar results were obtained from the T40 and T50 blends. In Fig. 2(b), we show the temperature dependence of the scattering data obtained from the P35 blend at 0.01 kbar. Again, we see an increase in the low-q scattering with decreasing temperature. The observed increase in the low-q scattering in Figs. 2(a) and 2(b) is a qualitative indication of an upper critical solution tempera-

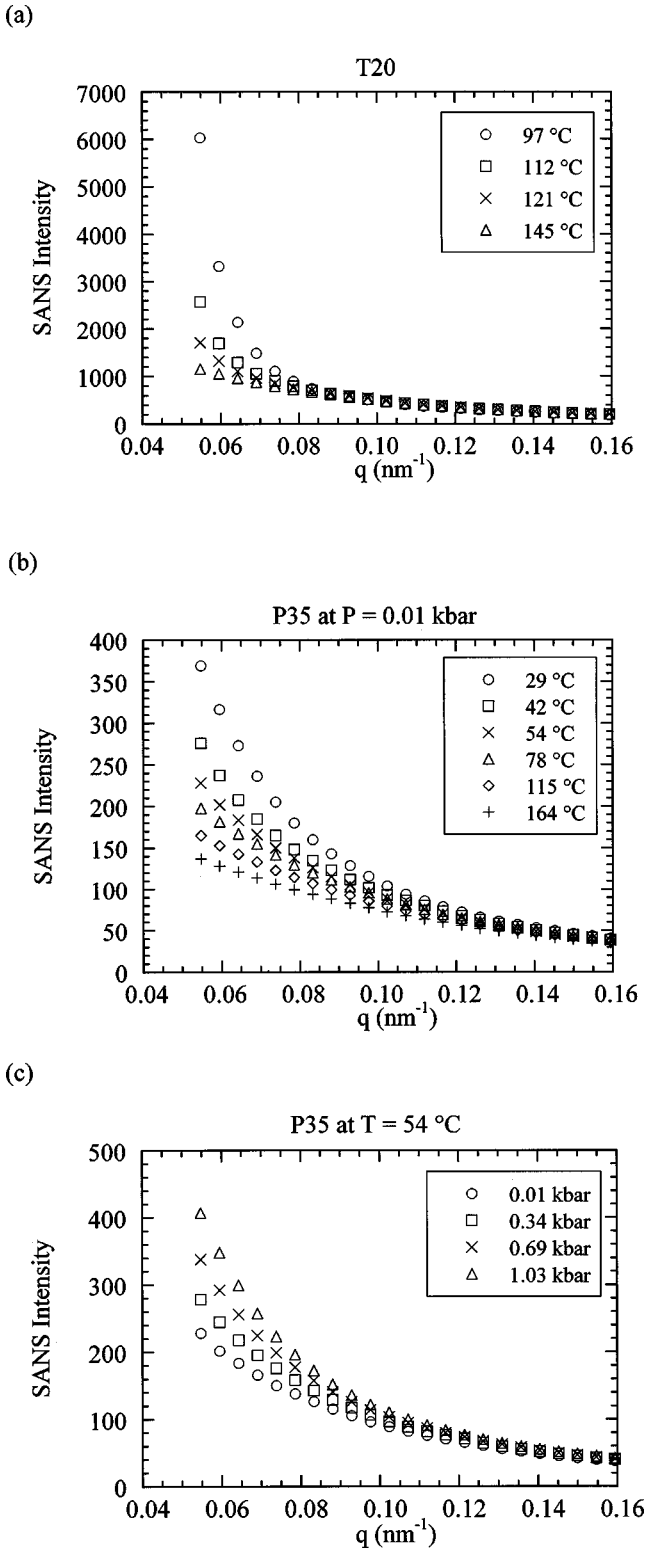

FIG. 2. The q dependence of the static SANS intensity, I, from (a) blend T20, and (b) blend P35, at selected temperatures. (c) The q dependence of the static SANS intensity, I, from blend P35, at selected pressures, and at a constant temperature of 54 °C.

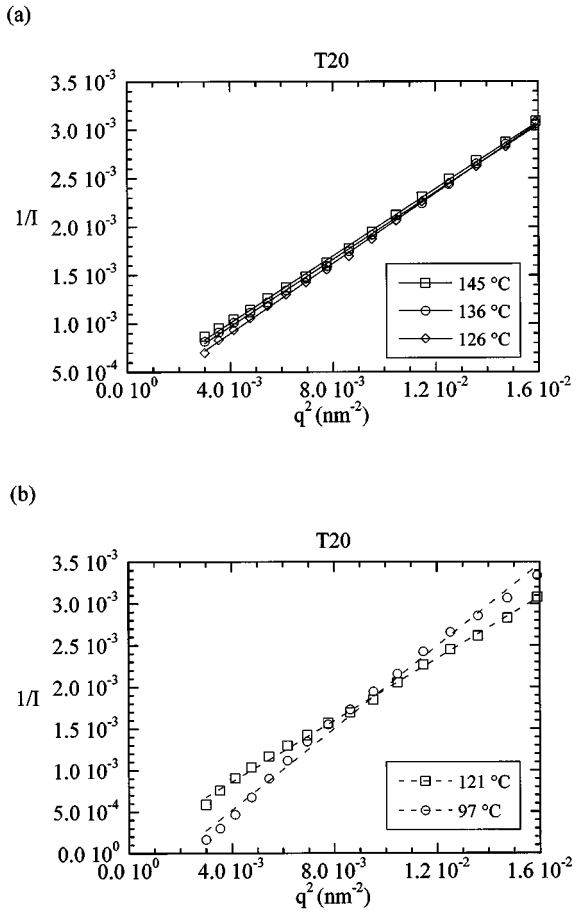

FIG. 3. The inverse of the scattered intensity, $1/I$, vs q^2 at various temperatures, (a) above the estimated binodal temperature, and (b) below the estimated binodal temperature for blend T20. The solid and dashed lines are the least-squares fits through the data.

ture (UCST), i.e., the blends are single phase above the binodal temperature, T_b. The effect of increasing the pressure at a constant temperature is shown in Fig. 2(c), where we show $I(q)$ obtained from the P35 blend at pressures ranging from 0.01 to 1.03 kbar, at a fixed temperature of 54 °C. It is apparent that increasing pressure has the same qualitative effect as decreasing temperature. The blend P35 thus exhibits a lower critical solution pressure (LCSP), i.e., this blend is single phase below a certain critical pressure, P_b. The trends with temperature and pressure are consistent with previous thermodynamic studies on PMB/PEB/PMB–PEB blends;[31–34,45] see Fig. 1.

In Fig. 3(a), we show the low-q scattering data from the blend T20 at $T \geqslant 126\,^{\circ}\mathrm{C}$ in the Zimm format, $1/I$ vs q^2. The lines in Fig. 3(a) represent least-squares fits through the data. It is apparent that the scattering profiles from the blend T20 at $T \geqslant 126\,^{\circ}\mathrm{C}$ are consistent with the Zimm equation (standard deviation at $126\,^{\circ}\mathrm{C} = 2.0 \times 10^{-5}$). This is typical of single-phase blends.[46] In Fig. 3(b), we show the low-q scattering data from the same blend (T20) at $T < 126\,^{\circ}\mathrm{C}$ in the Zimm format. The dashed lines in Fig. 3(b) represent least-squares fits through the data. Systematic deviations between the Zimm equation and the data can clearly be seen at $T < 126\,^{\circ}\mathrm{C}$ (standard deviation at $121\,^{\circ}\mathrm{C} = 3.4 \times 10^{-5}$) as is normally found for phase separated blends.[46]

The scattering intensity as $q \to 0\,(I_0)$ can be estimated by extrapolating the straight lines in Figs. 3(a) and 3(b). For consistency, the data in the range of $0.003 \leqslant q^2 \leqslant 0.016\,\mathrm{nm}^{-2}$ was used at all temperatures, regardless of the

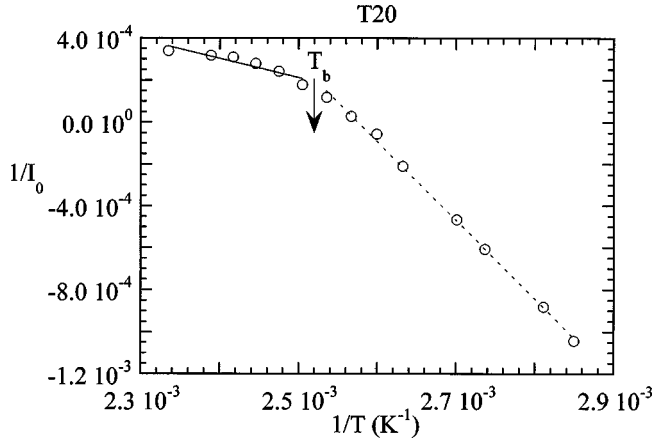

FIG. 4. The extrapolated inverse scattered intensity at $q=0$, $1/I_0$, vs $1/T$ for sample T20. The lines are determined by the least-squares procedure described in the text. The median between the lowest temperature of the high T set and the highest temperature of the low T set determines the binodal temperature indicated by T_b. Extrapolation of the solid line to $1/I_0=0$ determines the spinodal temperature, T_s.

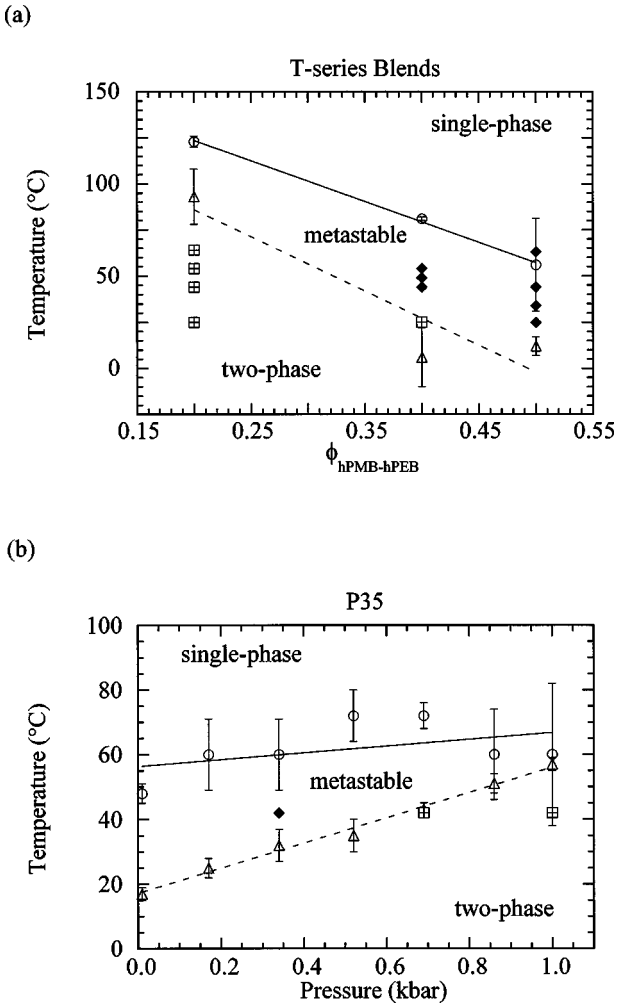

FIG. 5. (a) The phase diagram for *h*PMB/*d*PEB/*h*PMB–*h*PEB polymer blends (T20, T40, T50) at atmospheric pressure. (b) The phase diagram for blend P35 at elevated pressures. The solid lines represent least-squares fits through the binodal data points while the dashed lines represent least-squares fits through the spinodal data points. The diamonds and hatched squares indicate the temperatures and pressures at which the phase separation kinetics were studied. The diamonds indicate systems that exhibited nucleation and growth. The hatched squares indicate systems that exhibited spinodal decomposition.

goodness of the fit. The extrapolated value of $1/I_0$ is negative at $T<116\,^{\circ}\mathrm{C}$ [e.g., see the 97 °C data in Fig. 3(b)]. Of course, the true value of I_0 must be positive. The negative (extrapolated) values of I_0 are due to the presence of large phase separated domains that scatter at q values lower than the low-q limit of our instrument in configuration A.

In Fig. 4, we plot $1/I_0$ versus the reciprocal of absolute temperature $(1/T)$. One expects a linear dependence between $1/I_0$ and $1/T$ in the single-phase region.[47] In contrast, we see a clear break in the $1/I_0$ vs $1/T$ plot of the blend T20 (Fig. 4). Two linear regimes, represented by dashed and solid lines, are evident. The two lines were obtained by a fitting procedure wherein the data were divided into two groups (low T and high T) and a least-squares line was drawn through each of the sets. The point of division between the low T and high T regimes was varied systematically. The pair of lines, which minimized the sum of the square of the residuals, were chosen to describe the data. The binodal temperature (T_b) is assumed to be the median temperature between the lowest temperature of the high T data set and the highest temperature of the low T data set. For the blend T20, we obtain $T_b=123\pm3\,^{\circ}\mathrm{C}$. The stability limit, i.e., spinodal temperature (T_s), for T20 is obtained by extrapolating the straight line obtained in the single-phase regime (the solid line in Fig. 4) to the point where $1/I_0=0$. As a result, the spinodal temperature is estimated at $93\pm15\,^{\circ}\mathrm{C}$ for the blend T20.

The static SANS data from the blends T40, T50, and P35 were analyzed by the same procedure as described above for T20. The reported T_b values were obtained by the two least-squares lines approach and the T_s values were obtained by extrapolating the high T branch of the $1/I_0$ vs $1/T$ plot. In the case of P35, the procedure for obtaining T_b and T_s was repeated at elevated pressures. In all of the samples, at temperatures above T_b, the scattering profiles were independent of thermal history. However, at temperatures below T_b, we found that the scattering profiles did depend on thermal history. This is expected, because the two-phase morphology obtained in a given blend will depend on thermal history. The data in Fig. 4 were obtained while sample T20 was heated from room temperature to 155 °C. The differentiation between the high T and low T regimes was sharper for T40 than that shown in Fig. 4, while for T50 and P35 it was weaker.

The binodal and spinodal temperatures of blends T20, T40, and T50 are summarized in Fig. 5(a), where we show a phase diagram for *h*PMB/*d*PEB/*h*PMB–*h*PEB blends with $\phi_{\mathrm{PEB}}/\phi_{\mathrm{PMB}}=0.34$ in the $T-\phi_{h\mathrm{PMB}-h\mathrm{PEB}}$ plane. The pressure dependence of the binodal and spinodal temperatures of the blend P35 is shown in Fig. 5(b). In Figs. 5(a) and 5(b), the binodal and the spinodal temperatures are represented by solid and dashed lines, respectively. The diamonds and hatched squares in Figs. 5(a) and 5(b) represent the temperatures and pressures at which the phase transition kinetics were examined. The distinction between diamonds and hatched squares will be explained below.

Determining the equilibrium properties (binodal and

spinodal points) of our blends is not straightforward due to slow kinetics. In blends of lower molecular weight compounds, the binodal curve can simply be located by determining the temperature and pressure at which the blends become cloudy (the ''cloud point''). Most of our blends do not become cloudy even after they have been at atmospheric conditions for several years. All of the blends studied here are deep in the two-phase region at room temperature and pressure. It is evident that slow kinetics, the very feature that enables kinetic measurements during the early stages of nucleation, hinders the determination of equilibrium properties.

The T-series samples were annealed at 250 °C (deep in the single-phase region) for a minimum of 4 h in a vacuum oven. The samples were then rapidly transferred to a temperature controlled sample stage in the neutron beam. It took approximately 3 min to transfer the sample from the oven to the sample stage. The SANS data acquisition was started as soon as the sample was placed in the sample stage. Time zero ($t=0$) is defined as the time at which the time-resolved SANS measurements began. The time required for the sample temperature to reach quench temperature (within 1 °C) was estimated to be about 5 min. The P35 blend was first annealed at 0.01 kbar at 78 °C (deep in the single-phase region) in the pressure cell, and then cooled to 42 °C at 0.01 kbar. All of the kinetics experiments, in which increased pressure induced phase separation, were conducted at 42 °C. After equilibration at 42 °C and 0.01 kbar, the sample pressure controller was set to the experimental pressure. Time zero ($t=0$) for the pressure quenches is defined to be the time at which the pressure controller setting was changed.

In the pressure quench experiments, the annealing step was conducted in the pressure cell while it was in the neutron beam. We were thus able to obtain data just before the quench ($t=0^-$) in the single phase region and just after the quench ($t=3$ min). In addition, the sample could be cycled between the different regions of the phase diagram with relative ease, as we show below.

B. Reversibility of phase separation

We now discuss the time-resolved SANS data obtained in configuration B. In Fig. 6(a), we show SANS profiles obtained from the sample P35 at 42 °C, after the blend was subjected to a pressure quench from 0.01 to 0.69 kbar. We see a significant increase in the scattering intensity due to phase separation. We let the phase separation proceed for over 10^3 min, and then we depressurized the sample to 0.01 kbar. The time dependence of the scattering profiles after depressurization are shown in Fig. 6(b). Time zero, for the depressurization data set in Fig. 6(b), is defined to be the time when the pressure controller setting was changed to 0.01 kbar. The scattering intensity at all accessible q values decreases with increasing time, indicating dissolution of the phase separated structure.

The phase diagram for P35 in Fig. 5(b) indicates that at $T=42$ °C and $P=0.01$ kbar, the sample is near the border between the single-phase regime and the two-phase regime, while at $T=42$ °C and $P=0.69$ kbar, the sample is deep within the two-phase region. These assignments were based

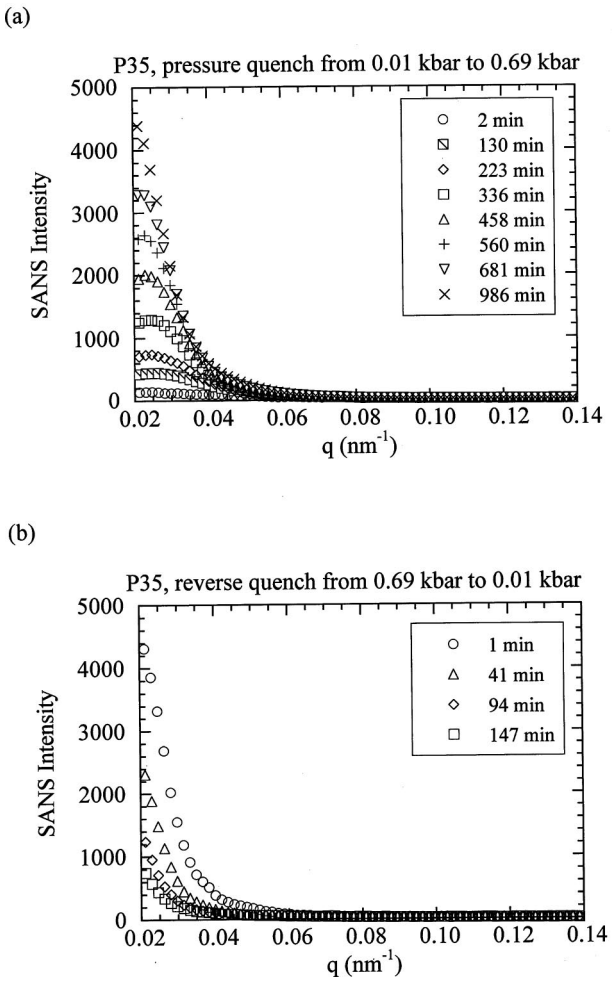

FIG. 6. Time dependence of the SANS profiles from blend P35. (a) Pressure quench from 0.01 to 0.69 kbar, and (b) is the reverse pressure quench from 0.69 to 0.01 kbar.

on static SANS data. The time-resolved data in Figs. 6(a) and 6(b) confirm these results. In particular, they indicate clearly that at $T=42$ °C and $P=0.01$ kbar, the sample P35 is in the single-phase regime. If we had not crossed a phase boundary when the sample was depressurized from 0.69 to 0.01 kbar, then there would not be a driving force for the dissolution of the two-phase morphology obtained at 0.69 kbar. The data in Figs. 6(a) and 6(b) also indicate that it is relatively easy to reverse phase separation in our blends. Despite the fact that at $P=0.69$ kbar, P35 is well within the two phase boundary, and at $P=0.01$ kbar, P35 is close to the phase boundary, the dissolution kinetics are much faster than the phase separation kinetics. The reason for this disparity is not clear. The two-phase structure that took approximately 10^3 min to develop was well on its way to complete dissolution after only 150 min. The ease with which phase separation can be reversed in these systems was crucial, because it enabled repeated measurements on the same sample.

C. Quenches into the spinodal region

Typical SANS profiles obtained after quenches into the spinodal region are shown in Fig. 7. The results for a quench to 63 °C for the T20 sample are shown in Fig. 7(a). A scat-

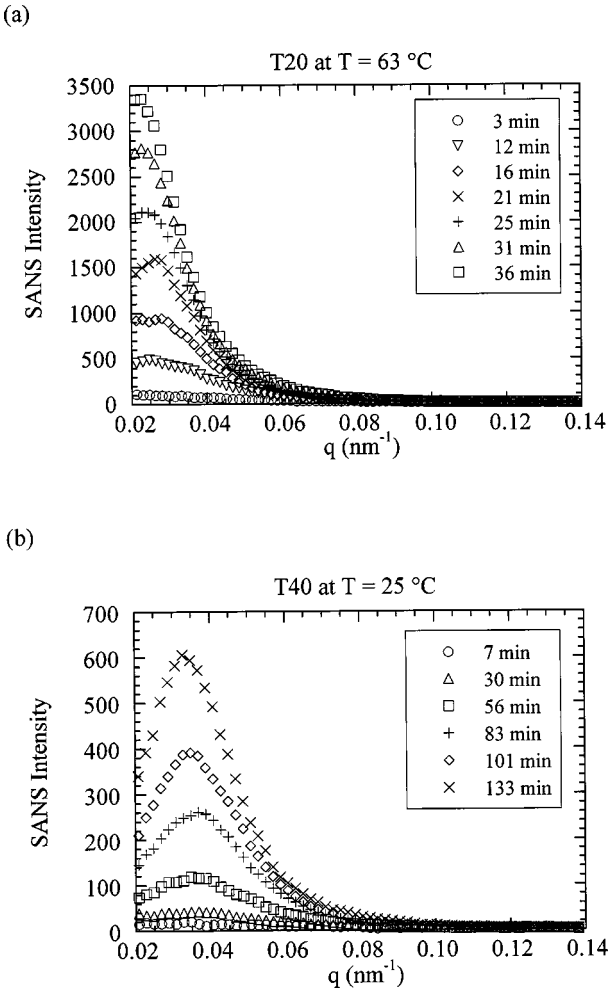

FIG. 7. SANS intensity vs scattering vector at selected times during spinodal decomposition. (a) Sample T20 at 63 °C, and (b) sample T40 at 25 °C.

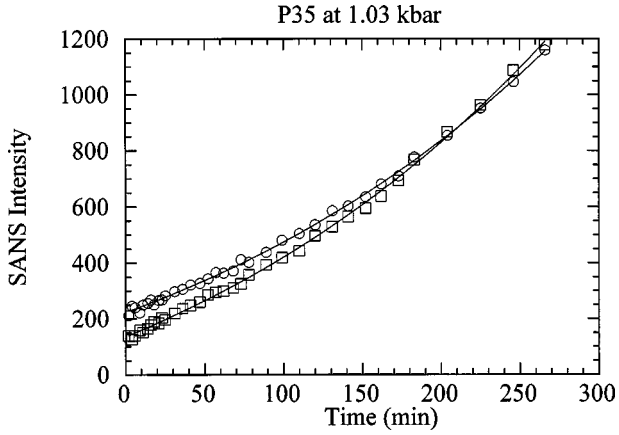

FIG. 8. Analysis of the spinodal decomposition data for the P35 blend at 1.03 kbar. The solid curves are least-squares fits of the data to the Cahn–Hilliard–Cook theory at $q=0.023\,\mathrm{nm}^{-1}$ (the open circles) and at $q=0.033\,\mathrm{nm}^{-1}$ (the open squares).

tering peak develops during the early stages at $q=0.028\,\mathrm{nm}^{-1}$. At times, $t>16$ min, the location of the scattering peak in q space, q_m, decreases with time, indicating the start of the intermediate stage of spinodal decomposition. The early stage of spinodal decomposition in sample T20 at 63 °C is completed relatively rapidly (16 min) due, mainly, to the large depth of the quench [see Fig. 5(a)]. In Fig. 7(b), we show the scattering profiles obtained from the T40 blend at 25 °C at selected temperatures. The early stage of spinodal decomposition during this experiment lasted for 83 min wherein a time-independent q_m is observed. At later times, q_m decreases with time, as was the case for sample T20 shown in Fig. 7(a).

The data obtained from quenches represented by the hatched squares in Figs. 5(a) and 5(b) [e.g., P35 at 0.69 kbar—Fig. 6(a), T20 at 63 °C—Fig. 7(a), and T40 at 25 °C—Fig. 7(b)] exhibited classic signatures of spinodal decomposition. The data obtained during the early stages of these quenches (before q_m decreased with time) were analyzed using the Cahn–Hilliard–Cook theory. In some cases, the early stage of spinodal decomposition was too rapid and thus the Cahn–Hilliard–Cook analysis could not be applied. In this theory,[2,48] the time dependence of the structure factor, $S(q,t)$, which is proportional to the scattered intensity profile, $I(q,t)$, is given by

$$I(q,t)\propto S(q,t)=S_x(q)+[S(q,0)-S_x(q)]\exp[\Lambda q^2 t], \qquad (2)$$

where $S_x(q)$ is the virtual structure factor, and Λ is the Onsager coefficient. Typical least-squares fits of the data to Eq. (2) are given in Fig. 8, where the time dependence of I at selected q values from P35 at 1.03 kbar are shown. The signatures of spinodal decomposition observed in the blends T20, T40, and P35 were identical to those observed in binary polymer blends.[8] In a previous publication,[17] we analyzed time-resolved SANS data obtained in the spinodal decomposition region from a different set of PMB/PEB/PMB–PEB bends. The data obtained from the present set of blends were qualitatively similar to the previously published data. We therefore do not discuss these data in any detail. The main purpose of presenting the data in Figs. 7 and 8 was to compare these data with the data obtained after quenches into the nucleation regime. These quenches are represented by the closed diamonds in Figs. 5(a) and 5(b).

D. Role of the block copolymer

Before discussing the time-resolved data obtained during nucleation, it is important to establish the role of the block copolymer in our multicomponent blends. In phase-separated mixtures of two homopolymers and a block copolymer, the block copolymer can exhibit three different types of behavior.[49,50] It could (1) serve as a polymeric common solvent that is uniformly distributed throughout the sample, or (2) serve as a surfactant and segregate to the interface between coexisting homopolymer-rich phases, or (3) form a separate, copolymer-rich phase. In most studies on mixtures of two homopolymers and a block copolymer,[51] the block copolymers serve as surfactants. However, evidence for all three types of behavior have been obtained experimentally.[52] For symmetric blends of two homopolymers, A and B ($\phi_A=\phi_B$) with $\chi N_A\approx\chi N_B\approx 2$, and a symmetric $A-B$ diblock copolymer it has been demonstrated that the transition from

common solvent-to-surfactant behavior occurs when χN_{A-B} is about 12.[38,40–42,50,52] In the PMB/PEB/PMB–PEB blends studied in this paper, $\chi N_{\mathrm{PMB-PEB}}$ is in the vicinity of 4. This is well below the threshold for interfacial activity of the copolymer. Similarly, the formation of copolymer-rich phases occurs at χN_{A-B} values significantly greater than 4.[49] We thus expect the PMB–PEB block copolymer to behave like a polymeric common solvent. In this scenario, the phase separation results in PMB-rich and PEB-rich macrophases, and the PMB–PEB block copolymer is uniformly distributed in both phases. If we assume that the blend is incompressible, then the spatial variation of homopolymer concentrations, $\phi_{\mathrm{PMB}}(\mathbf{r})$ and $\phi_{\mathrm{PEB}}(\mathbf{r})$ must satisfy the relationship $\phi_{\mathrm{PMB}}(\mathbf{r}) + \phi_{\mathrm{PEB}}(\mathbf{r}) = \text{constant}$. In the past,[17] we have referred to such blends as pseudobinary blends because they are expected to behave like binary blends of simple liquids [where $\phi_{\mathrm{PMB}}(\mathbf{r}) + \phi_{\mathrm{PEB}}(\mathbf{r}) = 1$].

In order to study the distribution of the block copolymer chains, we prepared a sample that we call T40D (see Table II), which is identical to T40 in most respects. Both blends contain 40 vol % PMB–PEB block copolymer and the ratio $\phi_{\mathrm{PEB}}/\phi_{\mathrm{PMB}}$ is 0.34. Both blends contain one deuterium labeled species. In the blend T40, the labeled species is the PEB homopolymer, while in the blend T40D, the labeled species is the PMB–PEB block copolymer. We expect the qualitative behaviors of samples T40 and T40D to be identical. Based on previous studies,[17,34] we can assert that switching deuterium labels from one component to another has little effect on the thermodynamics of these PMB/PEB/PMB–PEB blends with 40 vol % block copolymer. Given that blend T40 at 44 °C is located deep in the two-phase region [Fig. 5(a)], we expect the sample T40D to also exhibit phase separation at 44 °C. However, since there is no scattering contrast between the *h*PMB and *h*PEB homopolymers in the T40D blend (see Table I), changes in the distribution of these two components will not result in an increase in the scattering intensity. The scattering from T40D will evolve with time only if the distribution of *d*PMB–*d*PEB chains in the sample changes with time.

In Fig. 9, we show the SANS profiles from T40D at $T = 44\,^{\circ}\mathrm{C}$ at selected times. The scattered intensity is relatively weak and independent of time for 1000 min. This is in sharp contrast to sample T40 wherein a 400-fold increase in the scattering intensity was observed in 109 min (Fig. 9 inset). The time independence of the scattering data in Fig. 9 indicates this blend exhibits pseudobinary behavior. These experiments confirm conclusions based on theoretical arguments that were presented earlier in this section. Similar results were reported in a previous study of phase separation in PMB/PEB/PMB–PEB mixtures.[17] Based on the data in Fig. 9, previous experimental results,[36,38–42] and theory[49,50] we conclude that the block copolymer is uniformly distributed during all stages of the phase separation process in all of the blends examined in this paper.

The main objective of this paper is to study the clustering of homopolymer chains during nucleation. We do this in the remainder of this paper.

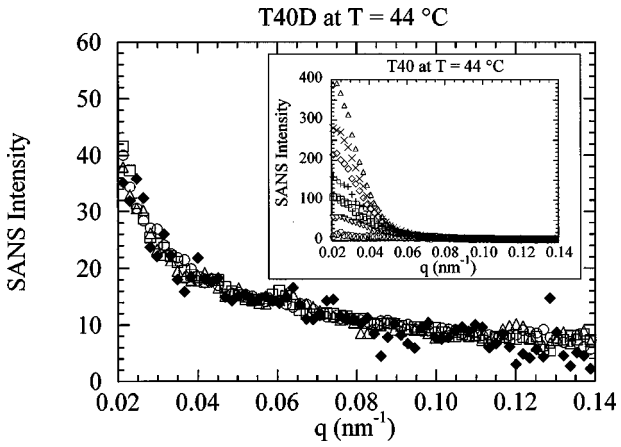

FIG. 9. SANS intensity vs scattering vector at selected times from blend T40D at 44 °C. Solid diamonds: $t = 3$ min; open circles: $t = 225$ min; open squares: $t = 439$ min; open triangles: $t = 1193$ min. The lack of change in the scattering intensity from T40D indicates that the block copolymer is uniformly distributed in the coexisting PEB- and PMB-rich phases. Inset: SANS intensity vs scattering vector at selected times from blend T40 at 44 °C. Circles: $t = 4$ min; upside down triangles: $t = 48$ min; squares: $t = 69$ min; plus signs: $t = 80$ min; diamonds: $t = 90$ min; crosses: $t = 99$ min; triangles: $t = 109$ min. The change in scattering intensity from T40 indicates the formation of PEB- and PMB-rich phases.

E. Three stages of nucleation

The time dependence of the SANS profiles obtained from samples T40, T50, and P35 are shown in Figs. 10, 11, and 12, respectively. We have left out sample T20, because all of the quenches were located deep in the spinodal region [Fig. 5(a)]. The differences between the time-resolved SANS data obtained during spinodal decomposition (discussed above), and those obtained during nucleation can be seen by comparing data obtained from P35 at 1.03 kbar [Fig. 12(a)] and at 0.34 kbar [Fig. 12(c)]. An obvious difference between the two sets of data is the presence of a scattering peak in the spinodal decomposition regime [Fig. 12(a)] at $q = q_{\max} \approx 0.03\,\mathrm{nm}^{-1}$, and the absence of a scattering peak in the nucleation regime [Fig. 12(c)].

In Fig. 13(a), we show the time dependence of the scattered intensity from P35 at a fixed $q = 0.021\,\mathrm{nm}^{-1}$ during spinodal decomposition ($P = 1.03$ kbar). The data obtained during the early stage ($t \leqslant 266$ min), designated by ''*E*,'' are in agreement with the Cahn–Hilliard–Cook theory. The solid curve in Fig. 13(a) represents a least-squares fit of Eq. (2) through the data obtained at $t \leqslant 266$ min. Systematic deviations between the $I(t)$ and the Cahn–Hilliard–Cook predictions are evident in the intermediate stage, designated by ''*I*'' in Fig. 13(a). The inset in Fig. 13(a) shows the pressure reading from the transducer closest to the sample after the set point on the pressure controller is changed. Changing the sample pressure from 0.01 to 1.03 kbar requires about 15 min. A sudden change in the sample pressure will result in a change in the sample temperature due to the Joule–Thompson effect. Migler and Han have shown that for typical polymer samples with 1 mm thickness, the sample temperature returns to the set temperature within 10 s.[53] The time scale required to enforce an isothermal pressure quench is thus considerably less than the time scale for phase sepa-

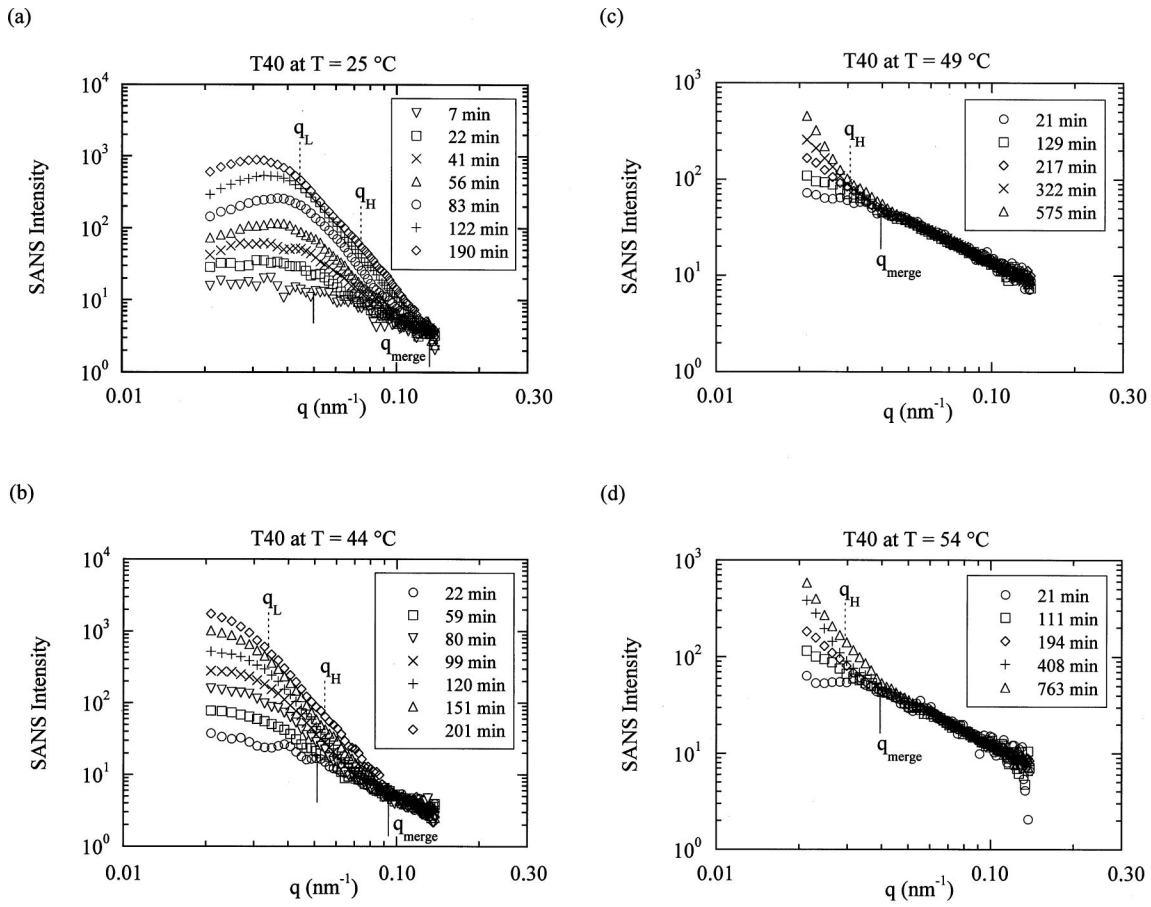

FIG. 10. Log–log plots of the SANS intensity vs scattering vector at selected times from blend T40 after temperature quenches: (a) quench to 25 °C, (b) quench to 44 °C, (c) quench to 49 °C, (d) quench to 54 °C. The solid and dashed lines show the positions of q_H and q_L at the earliest and latest times shown, respectively.

ration during the early stage of spinodal decomposition (266 min).

The time dependence of the scattered intensity from P35 at $q=0.021\,\mathrm{nm}^{-1}$ during nucleation ($P=0.34$ kbar) is shown in Fig. 13(b). This pressure quench from 0.01 to 0.34 kbar is accomplished in approximately 1 min [see the inset in Fig. 13(b)]. At very early times $t<\tau_F=98$ min, we find a relatively rapid increase in the scattering intensity during the 0.34 kbar quench. This is followed by a slower growth of the scattering intensity at times $\tau_F\leqslant t\leqslant\tau_E=618$ min. At longer times, $t>\tau_E$, the rate of phase separation, as measured by the time dependence of the SANS intensity, begins to increase. We refer to the first stage as the fluctuation relaxation stage (F) where $t<\tau_F$, the second stage as the early stage of nucleation (E) where $\tau_F\leqslant t\leqslant\tau_E$, and the third stage as the intermediate stage of nucleation (I) where $t>\tau_E$; see Fig. 13(b). Linear fits through the I vs t data were used to identify the crossover from F to E, and E to I.[54]

The extent of phase separation can be quantified by computing the time dependence of the scattering invariant, I_{inv}

$$I_{\mathrm{inv}}=\int I(q)q^2\,dq. \tag{3}$$

The integration was performed over the entire q range $0.02\leqslant q\leqslant 0.14\,\mathrm{nm}^{-1}$ using the trapezoidal rule. We used the Integrate-Area function of the KALEIDAGRAPH for Windows, version 3.09 program. In Fig. 13(c), we show the time dependence of I_{inv} for P35 at 0.34 kbar. The three regimes of nucleation identified earlier in Fig. 13(b) are also shown in Fig. 13(c). The distinction between the F, E, and I stages are evident in the time dependence of I_{inv}. Note that the F, E, and I stages were identified using the scattered intensity at a single q value [Fig. 13(b)] while the data in Fig. 13(c) reflect a weighted average of scattering at all accessible q.

F. The fluctuation relaxation stage

Most of the samples exhibited a relatively rapid initial response after quenching into the metastable region; see Figs. 13(b) and 13(c). An obvious explanation for this initial response is the fact that it takes a finite amount of time to change the sample temperature or pressure from its initial value in the one-phase region to its final value in the two-phase region. However, it appears that this is not the case. For the 0.34 kbar quench of the sample P35 this ''initial'' response is spread out over 98 min. This is a much longer time scale than is required to effect a change in sample pressure from 0.01 to 0.34 kbar, which is 1 min. (Joule–Thompson effects will dissipate in less than 5 s.[53]) We propose that the relatively rapid increase in the SANS scattering observed at times less than $t<\tau_F$ reflects the response of the metastable, single-phase fluid to the pressure quench. The

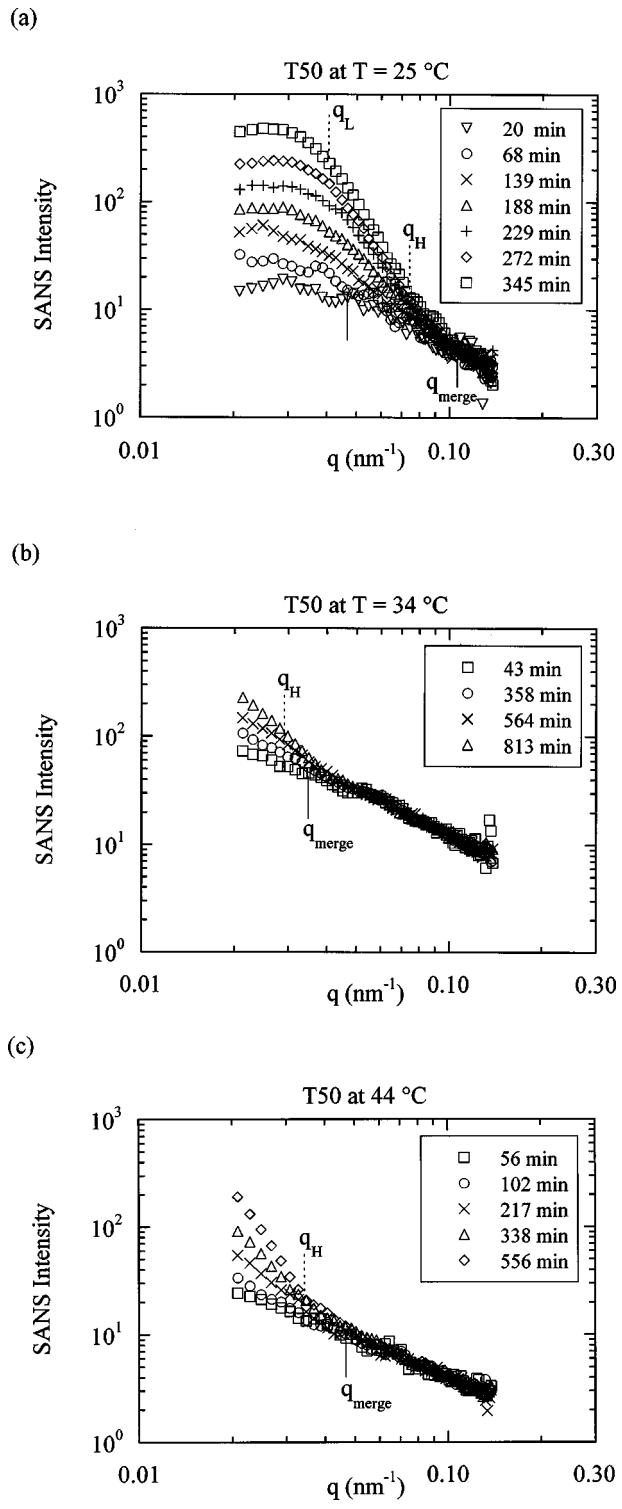

FIG. 11. Log–log plots of the SANS intensity vs scattering vector at selected times from blend T50 after temperature quenches: (a) quench to 25 °C, (b) quench to 34 °C, (c) quench to 44 °C. The solid and dashed lines show the positions of q_H and q_L at the earliest and the latest times, shown, respectively.

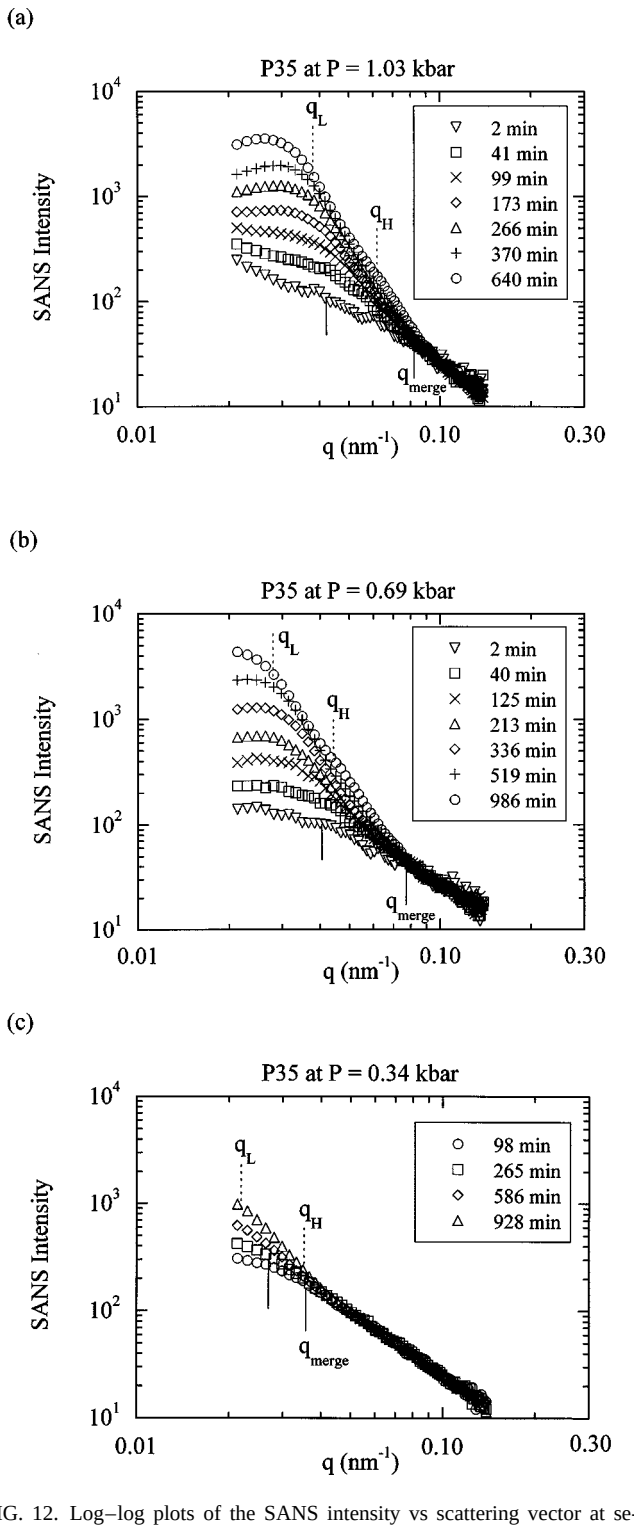

FIG. 12. Log–log plots of the SANS intensity vs scattering vector at selected times from blend P35 after pressure quenches: (a) quench to 1.03 kbar, (b) quench to 0.69 kbar, (c) quench to 0.34 kbar. The solid and dashed lines show the positions of q_H and q_L at the earliest and the latest times shown, respectively.

response of polymer blends quenched from one equilibrium state to another was studied by Feng *et al.*[55] We believe that the initial response of our polymer blends is analogous to the process studied by Feng *et al.*, except for the fact that the final state in our case is metastable. We thus refer to the first process in our nucleation experiments as the fluctuation relaxation process (F). The fluctuation relaxation process is not observed during spinodal decomposition [e.g., P35 during 1.03 kbar quench—Fig. 13(a)]. Similar results were obtained in other studies of spinodal decomposition in polymer blends, e.g., Refs. 7–9. We set $\tau_F = 0$ in the spinodal decomposition regime.

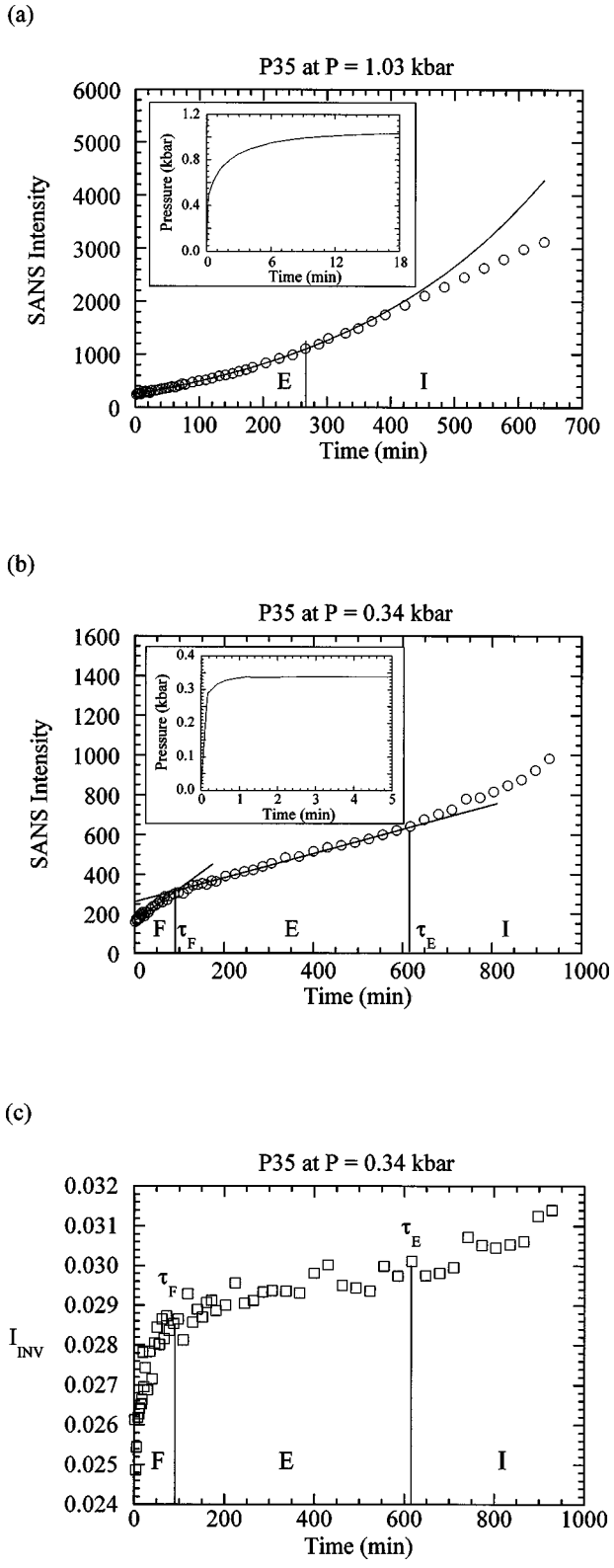

FIG. 13. Characteristics of the different stages of phase separation. *F* denotes the fluctuation relaxation stage, *E* denotes the early stage, and *I* denotes the intermediate stage. τ_F is the end of the fluctuation relaxation stage (*F*), and τ_E is the end of the early stage of nucleation (*E*). (a), (b) The SANS intensity vs time at $q=0.021\,\mathrm{nm}^{-1}$ for the P35 blend after pressure quenches. (a) Quench to 1.03 kbar. The solid line represents the Cahn–Hilliard–Cook fit to the data. The vertical line indicates the end of the early stage for spinodal decomposition (*E*). (b) Quench to 0.34 kbar. (c) The time dependence of the scattering invariant, I_{inv} during the 0.34 kbar quench. The inset in (a) and (b) show the time dependence of the sample pressure during these quenches.

TABLE III. Start and end times (τ_F and τ_E, respectively) for the early stage of nucleation and growth.

Quench temperature or pressure	P35		T40		T50	
	τ_F (min)	τ_E (min)	τ_F (min)	τ_E (min)	τ_F (min)	τ_E (min)
25 °C					19.5	149
34 °C					43	280
44 °C			22	42	56	181
49 °C			21	76		
54 °C			21	111		
0.34 kbar	98	618				

The fluctuation relaxation process is observed in the nucleation regime, because the phase separation process is relatively slow. We conclude that, regardless of the quench type (temperature quench versus pressure quench), the rapid increase in the scattering intensity observed in the very early stages of the quenches to the nucleation regime is due to the fluctuation relaxation process. The time required to complete the fluctuation relaxation process, τ_F, in each of the quenches to the metastable region, and the times required to complete the early stage of nucleation, τ_E, are given in Table III. We find that in most cases τ_F and τ_E increase with decreasing quench depth. In general, these time scales will depend on thermodynamic and viscoelastic factors. In our limited experimental window, τ_F and τ_E are dictated by thermodynamic factors. Since we are primarily interested in the nucleation process, we do not discuss the data at $t<\tau_F$ in the remainder of the paper.

G. The early and intermediate stages of nucleation

Let us go back to the data obtained from sample T40 (Fig. 10). The presence of a scattering peak during spinodal decomposition [Fig. 10(a)] indicates the presence of a periodic structure. The lack of a scattering peak [Figs. 10(b)–10(d)] during nucleation indicates that the emerging phase separated structure is characterized by a distribution of length scales. Examination of Figs. 10(a)–10(d) shows that for each quench, the scattering profiles at different times merge at a point that we depict by the symbol q_{merge}. The SANS intensity is independent of time in the range $q>q_{\mathrm{merge}}$. We begin by studying the SANS profiles at $q<q_{\mathrm{merge}}$. For sample T40 at 44 °C [Fig. 10(b)], at $t=201$ min, the scattered intensity decreases sharply with increasing q in the range $0.033\,\mathrm{nm}^{-1}<q<0.055\,\mathrm{nm}^{-1}$. The q dependence of I in this region can be approximated by a power law $I\sim q^{-d}$. We define q_L and q_H to be the lower and upper bounds, respectively, over which power law behavior is observed.[56]

A crossover in the q dependence of I is evident at $q\approx q_L$ [$q_L=0.033\,\mathrm{nm}^{-1}$ in T40 at 44 °C at 201 min; see Fig. 10(b)]. In the range, $q<q_L$, the scattered intensity appears to approach a q-independent plateau. The solid lines in Fig. 10 indicate the position of q_L and q_H at τ_F, which is the earliest time shown in the figures. The dashed lines show the positions of q_L and q_H at the last time shown in the figures. The

crossover from power law behavior to an apparent plateau, $q<q_L$ [Fig. 10(b)] is typical of scattering from disordered systems such as polymer blends and solutions and particulate suspensions.[4] This crossover is an indication of the characteristic length scale of the structure, $\xi(\xi\approx 1/q_L)$ and it represents the approach toward Zimm scattering in the $q\xi\ll 1$ limit. The characteristics of the SANS data obtained from samples T50 and P35 were similar to that of sample T40 (compare Fig. 10 with Figs. 11 and 12). The characteristic scattering vectors, q_{merge}, q_L, and q_H in these samples were obtained using procedures that were identical to those used in the analysis of the T40 data.

A detailed analysis of the scattering profiles is possible in the case of quenches into the binodal region where q_L was identified (T40 at 44 °C, T50 at 25 °C, and P35 at 0.34 kbar). A number of simple models have been used to describe polymer mixtures.[4] The Ornstein–Zernike (OZ) equation is often used to analyze scattering profiles in the single-phase region while the Debye–Bueche (DB) equation is often used to analyze scattering profiles in the two-phase region. Since we have a blend that is transforming from a one-phase system to a two-phase system, it is not immediately obvious whether we should use the OZ equation or the DB equation. In Sec. III F we established that the system is single phase at the end of the fluctuation relaxation stage. We therefore expect the OZ equation to be applicable, at least during the very early stages of nucleation. The OZ equation for the scattering profile is given by

$$I(q)=\frac{I_0}{1+q^2\xi^2}, \tag{4}$$

where I_0, the extrapolated intensity as $q\to 0$, is proportional to the product of the scattering power and the average mass of the scatterers. In Fig. 14(a), we show data obtained after a temperature quench in sample T40 to 44 °C, while in Fig. 14(b) we show data obtained after a pressure quench for the sample P35 to 0.34 kbar. In both cases we restrict our attention to the early stage of nucleation ($\tau_F\leqslant t\leqslant\tau_E$) and to times where a significant number of data points were obtained in the $q<q_L$ range. The curves through the data in Fig. 14 are the least-squares fits to the OZ equation [Eq. (4)] with I_0 and ξ as free parameters. It is evident that the data after both temperature and pressure quenches are in reasonable agreement with the OZ equation.

The typical time dependence of the fitted OZ parameters (I_0 and ξ) during the early stage of nucleation is shown in Fig. 15. We show data obtained from T40, T50, and P35. Note the wide variety of time scales and length scales obtained during the early stages of nucleation in the different samples. In the T40 sample at 44 °C, the early stage lasts for 20 min and ξ increases from 30 to 40 nm. In the P35 sample at 0.34 kbar, the early stage lasts for 250 min in which time ξ increases from 50 to 150 nm. In Fig. 16, we show the relationship between ξ and I_0 for all of the data shown in Fig. 15. (The 25 °C quench on the T50 sample was performed twice). The time-dependent values of I_0 and ξ obtained from the different quenches were normalized by their values at the beginning of the early stage (τ_F). It is apparent

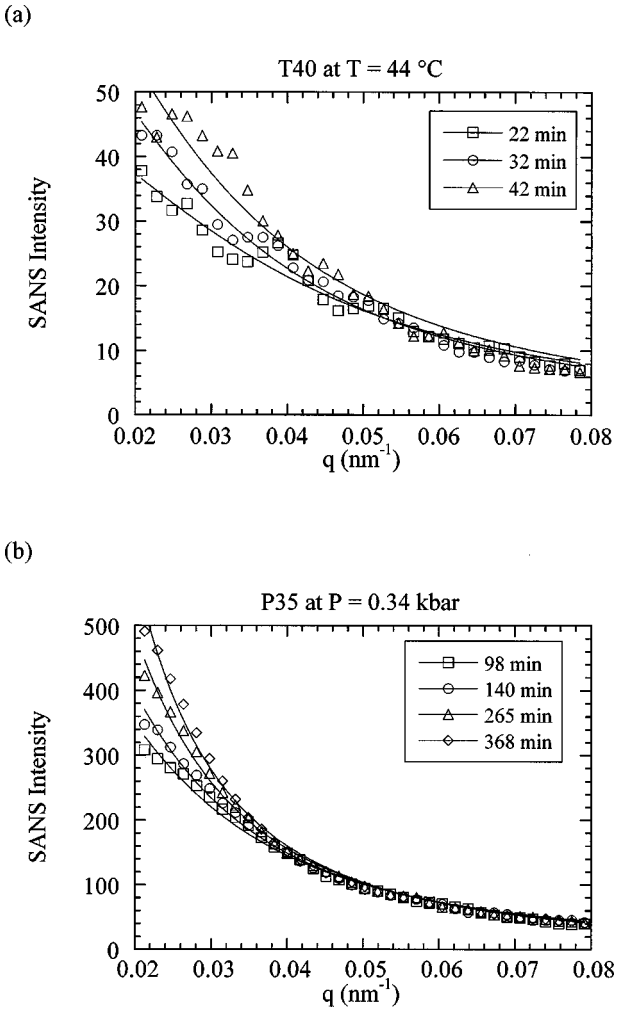

FIG. 14. SANS intensity vs scattering vector at selected times during the early stage of nucleation. (a) Blend T40 at 44 °C. (b) Blend P35 at 0.34 kbar. The solid curves are the Ornstein–Zernike [Eq. (4)] fits through the data.

that all of the data collapse onto a master line, consistent with the following scaling law:

$$\frac{\xi(t)}{\xi(\tau_F)}=\sqrt{\frac{I_0(t)}{I_0(\tau_F)}}. \tag{5}$$

The observed increase in the scattering intensity, during the early stage of nucleation, implies clustering of the labeled chains in the mixture. The $\xi\sim\sqrt{I_0}$ scaling is indicative of the nature of the clusters. In the mean-field limit, the scattering from concentration fluctuations in binary liquid mixtures (including polymer mixtures) obeys Eq. (5). We therefore conclude that the clusters formed during the early stage of nucleation cannot be distinguished from mean-field concentration fluctuations. The fact that ξ and I_0 increase with time (Figs. 15 and 16) implies that the concentration fluctuations grow during the early stages of nucleation. The observed scaling of ξ on I_0 [Eq. (5)] provides some justification for using the OZ equation.

The Ornstein–Zernike analysis was restricted to deep quenches wherein both q_L and q_H were within the accessible q window. It is not possible to conduct the same analysis of the data in the cases where q_L could not be identified, spe-

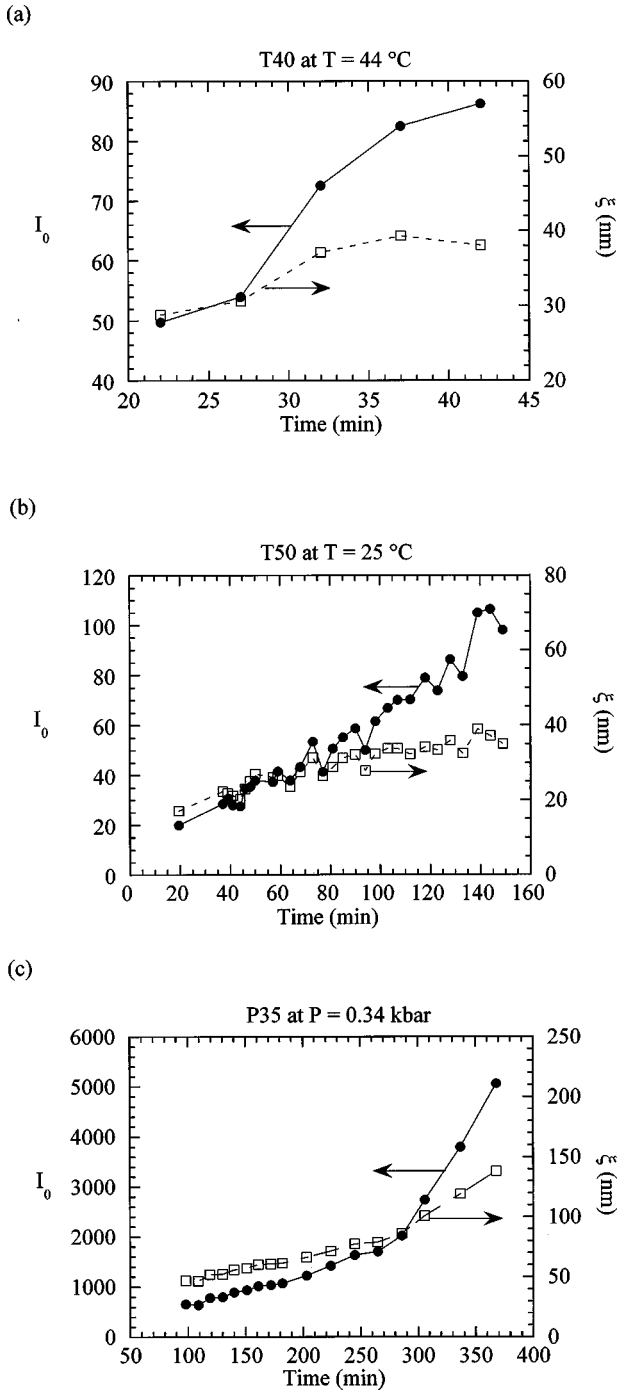

FIG. 15. The dependence on time of the Ornstein–Zernike parameters, I_0 (solid circles) and ξ (open squares). (a) Blend T40 at 44 °C, (b) blend T50 at 25 °C, and (c) blend P35 at 0.34 kbar.

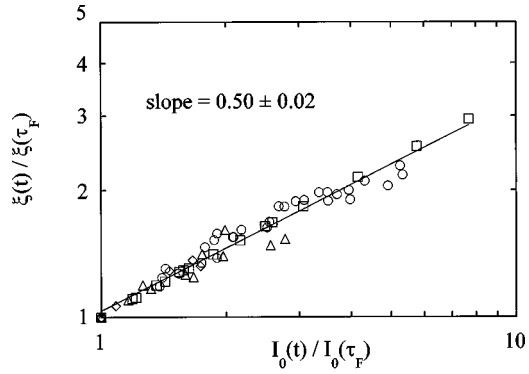

FIG. 16. The relationship between the Ornstein–Zernike parameters, I_0 and ξ, during the early stage of nucleation. Diamonds: blend T40 at 44 °C. Circles and triangles: two separate quenches of blend T50 to 25 °C. Squares: blend P35 at 0.34 kbar. I_0 and ξ were normalized by their values at the beginning of the early stage ($t=\tau_F$) for each of the quenches.

cifically the shallower quench depths [e.g., T40 at 49 and 54 °C, see Figs. 10(c) and 10(d)]. All microstructures must exhibit Zimm scattering in the limit of $q\xi \to 0$. The fact that we do not observe this limit at low-quench depths simply indicates that the characteristic length scale of the growing structures (ξ) is larger than the instrumental resolution.

Having established the origin of the scattering in the q range $q < q_L$, we move on to the $q_L \leqslant q \leqslant q_H$ regime where I scales as q^{-d}. This is sometimes called the intermediate q regime. The scattering profiles in this regime are related to the fractal dimension of the scatterers.[4] Least-squares power law fits were used to estimate d as a function of time and quench depth for each sample. For the cases where q_L could not be identified, we fit all of the I vs q data at $q \leqslant q_H$ to a power law $I \sim q^{-d}$, assuming that q_L lies behind the beam stop. Typical results of the fitting procedure are shown in Fig. 17(a) where we plot d versus time for the four quenches ($t > \tau_F$) performed on T40. We have included the data obtained at the largest quench depth (25 °C), the open triangles in Fig. 17(a), where T40 exhibited standard signatures of spinodal decomposition. In all of the cases the time dependence of d has a sigmoidal shape. At early times, d varies between 0.8 and 2. At later times, d increases, reaches a maximum value, and then decreases.

The value of d obtained during the early times are not reliable due to the relatively weak scattering intensity during this time. Incoherent scattering, which has not been subtracted from the measured signal, is probably important at large scattering vectors. As phase separation proceeds, and the scattering intensity increases, background subtraction is no longer important, and reliable values of d are obtained. In all of the cases, the fractal dimension of the phase separated structure increases as phase separation proceeds. It is clear from Fig. 17(a) that as $t \to \infty$, d will approach an asymptotic value between 3 and 4. In two phase systems with sharp interfaces, $I \sim q^{-3}$, in the $q\xi \approx 1$ regime (Kratky regime), and $I \sim q^{-4}$ in the $q\xi \gg 1$ regime (the Porod regime).[4] (Here ξ is the characteristic length scale of the phase separated structure.) Therefore, the increase in d from low initial values to values between 3 and 4 is consistent with the formation of a phase-separated structure. The fact that d is less than 3 during a significant portion of the nucleation process indicates that nucleation occurs via the formation of structures that are not compact. Mean-field concentration fluctuations, which we believe are responsible for nucleation, fall into this category.

The data in Fig. 17(a) suggests that increasing the quench depth in sample T40 simply results in a shift of the $d(t)$ data to the right. Note that the abscissa in Fig. 17(a) is $\log(t)$. The data are reminiscent of rheological data from homopolymers, wherein the time dependence of the stress relaxation modulus shifts to longer times as the temperature is

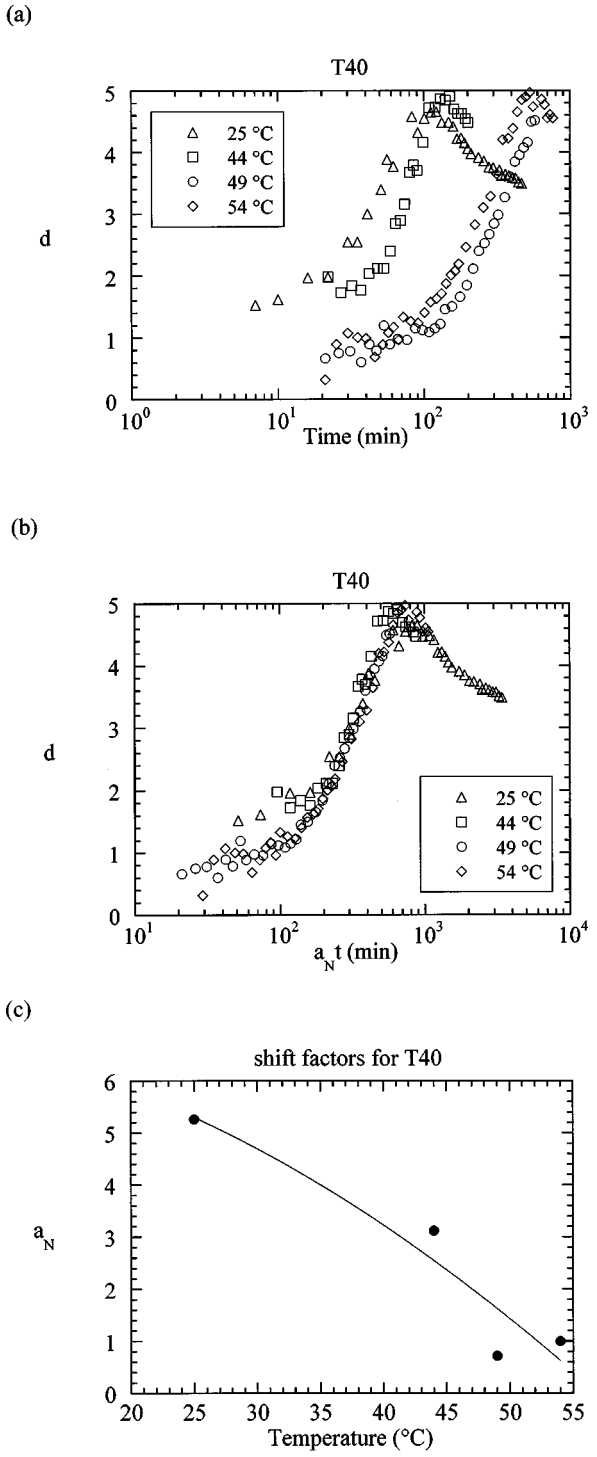

FIG. 17. Demonstration of the time–temperature superposition principle on data obtained from blend T40. (a) A plot of the exponent d vs log time for all of the quenches on the T40 blend. (b) The $d(t)$ data in (a) shifted along the horizontal (log time) axis to obtain best overlap with the 54 °C data. The abscissa is thus $\log(a_N t)$ where a_N is the nucleation shift factor. (c) The shift factor, a_N, vs temperature. The solid curve is a quadratic fit through the data.

lowered. The principle of time–temperature superposition has been established for collapsing rheological data at different temperatures.[57] We find that a similar principle can be applied to our nucleation data. Multiplying the time axis by a shift factor, a_N, results in a collapse of the $d(t)$ curves. This concept is tested in Fig. 17(b) where we plot d vs $a_N t$ for T40. The reference temperature (where a_N is set to unity) is 54 °C, for the T40 blend. Aside from the early time scatter, we observe a significant collapse of the time dependence of d [see Fig. 17(b)].

The temperature dependence of the shift factors (a_N) for the T40 sample is shown in Fig. 17(c). The value of $1/a_N$ may be considered as an estimate of the time scale for nucleation, relative to that observed at the reference temperature. The large values of a_N at lower temperatures thus imply that the nucleation process is more rapid at lower temperatures. The nucleation shift factors are different from the rheological shift factors because rheological time scales decrease with increasing temperature as a result of the increasingly rapid molecular motion. Of course, in our blends, molecular motion does slow down with decreasing temperature. However, the nucleation time scales in our experimental window appear to be dominated by quench depth, i.e., thermodynamics, rather than molecular mobility. A quadratic extrapolation of the shift factor data [Fig. 17(c)] suggests the existence of a point at which $a_N \rightarrow 0$. For the T40 sample this happens at 57 °C. A shift factor of zero implies that the nucleation process would require infinite time, i.e., time scales much larger than the experimental window (10^3 min). One may thus regard these points as binodal points determined by dynamical measurements. Our dynamical estimate of T_b of 57 °C in T40 is somewhat lower than that determined from static SANS (81 °C).

The time dependence of d obtained for samples T50 and P35 were similar to that obtained for T40. For completeness, Fig. 18(a) shows d vs $a_N t$ for P35 at a reference pressure of 0.34 kbar. We refer to this as time–pressure superposition. The pressure dependence of the shift factor a_N is shown in Fig. 18(b). The dynamical estimate of P_b in P35 at 42 °C is 0.2 kbar, while static SANS indicate that it is near 0 kbar [Fig. 5(b)]. In most cases a_N decreases as the binodal is approached [see Figs. 17(c) and 18(b)]. The $T=49$ °C quench of the sample T40 [Fig. 17(c)] and $T=34$ °C quench of sample T50 (see Fig. 11) are the only exceptions. We have no explanation for these deviations. We suspect that it reflects the delicate nature of nucleation near the binodal and our inability to exercise precise control over quenching conditions.

In both T40 and P35, the superposition principle was applied to data obtained during both spinodal decomposition and nucleation (Figs. 17 and 18). The ability to collapse all the quenches for a particular sample onto a master curve implies that the crossover from spinodal decomposition to nucleation is smooth. The lack of an abrupt change as one crosses the mean-field spinodal line, observed in samples T40 and P35, was anticipated by Binder.[19,20] To our knowledge there has not been any theoretical or experimental work that indicates this crossover would be manifested in time–temperature and time–pressure superposition principles.

The similarity of the data obtained at all quench depths in Fig. 17 suggests that the nucleating structures formed during the shallow quenches (e.g., T40 at 49 and 54 °C) are similar to those formed during deep quenches (e.g., T40 at

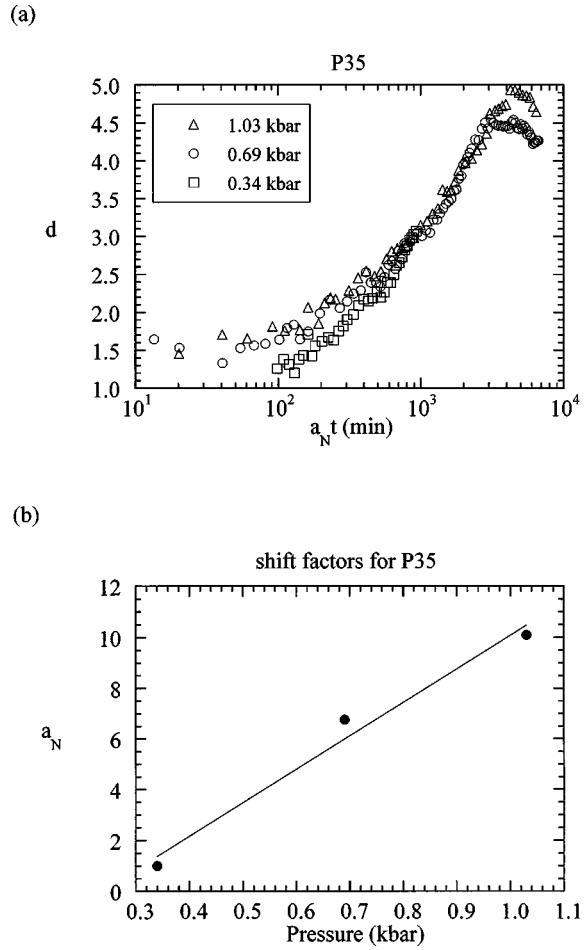

FIG. 18. Demonstration of the time–pressure superposition principle on data obtained from blend P35. The $d(t)$ data obtained from different quenches were shifted along the horizontal (log time) axis to obtain the best overlap with the 0.34 kbar data. (b) The shift factor, a_N, vs pressure. The solid line is a least-squares linear fit through the data.

25 and 44 °C). The nature of the nucleating structures can be gauged by examining I_{excess} defined as

$$I_{\text{excess}}(q,t) = I(q,t) - I(q,\tau_F), \quad t > \tau_F . \tag{6}$$

Our objective is to compare the nucleating clusters in sample T40 at 25, 44, 49, and 54 °C. One of the problems in making such a comparison is that the clusters change with time. It is therefore necessary to compare the nature of the clusters at equivalent times during the nucleation process. The nucleation shift factors, a_N, allow a clear definition of equivalent times. For example, if we are interested in the clusters formed during the 54 °C quench in T40 (the reference temperature for the shift factors) at 111 min, then the equivalent time during the $T=44\,^{\circ}\text{C}$ quench is at time $t = 111/a_N$ which is approximately 37 min. (We have ''rounded off'' the equivalent time to match the time at which the data were acquired.) Similarly, the equivalent time for $T=49\,^{\circ}\text{C}$ run is 155 min. We compare the scattering profiles obtained from T40 at equivalent times by examining the q dependence of I_{excess} on a log–log plot in Fig. 19. The scattering profiles were shifted horizontally to obtain the best collapse. In other words, the q axis is normalized by a fit parameter q_c. The values of q_c used in Fig. 19 are given in

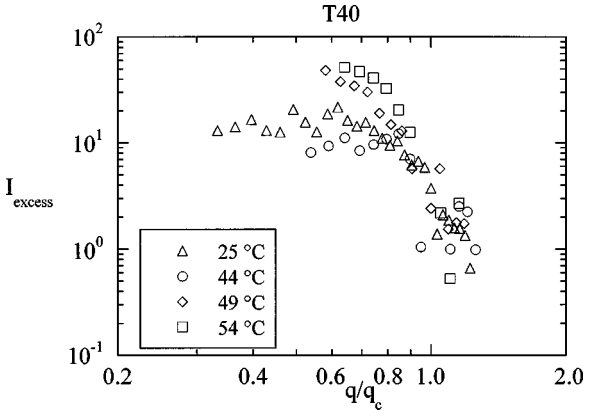

FIG. 19. I_{excess} at equivalent times vs a normalized q value for all of the quenches on the T40 blend. The open triangles are the 21 min data for the 25 °C quench, $q_c = 0.063\ \text{nm}^{-1}$, the open circles are the 37 min data for the 44 °C quench, $q_c = 0.039\ \text{nm}^{-1}$, the open diamonds are the 155 min data for the 49 °C quench, $q_c = 0.037\ \text{nm}^{-1}$, and the open squares are the 111 min data for the 54 °C quench, $q_c = 0.033\ \text{nm}^{-1}$.

the figure caption. The similarity of I_{excess} obtained at different quenches, at equivalent times, suggests that the structures formed in T40 at all quench depths are similar. The main distinction lies in the Zimm ($q\xi < 1$) regime. The data in Fig. 19 also indicated the lack of a sharp distinction between spinodal decomposition ($T=25\,^{\circ}\text{C}$) and nucleation ($T \geqslant 44\,^{\circ}\text{C}$).

In Figs. 17–19, we emphasize the similarity of the data obtained at different quench depths. Note that there are also important differences in the phase separation kinetics due to changes in quench depth. In Fig. 20, we show the time dependence of the scattering invariant I_{inv} for all of the quenches performed on T40. When the composition and the volume fraction of the coexisting phases reaches equilibrium, I_{inv} approaches a time-independent plateau. This is usually called the late stage of phase separation. The kinetics of phase separation at 25 °C (solid circles) were relatively rapid and the late stage was reached in approximately 200 min. It is clear from Fig. 20 that at lower quench depths, the late stages of phase separation lay outside the experimental window. We expect that near the binodal, the long time pla-

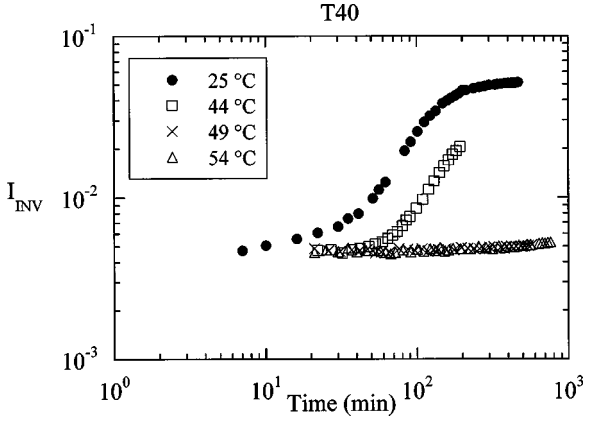

FIG. 20. The time dependence of the I_{inv} for all of the quenches on the T40 blend.

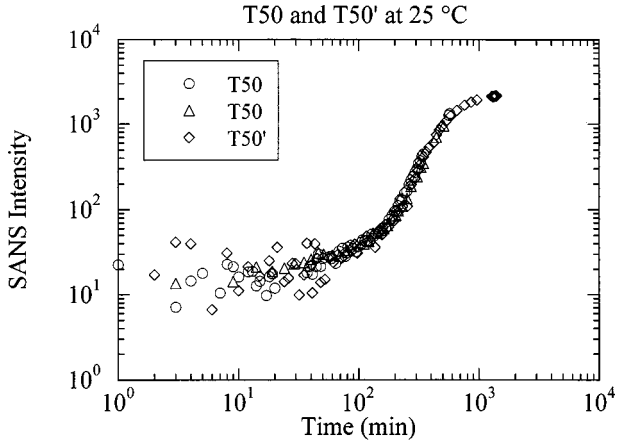

FIG. 21. The dependence of the SANS intensities on time at $q = 0.02\ \mathrm{nm}^{-1}$, for the three 25 °C quenches on blends containing 50 vol % diblock copolymer. Circles and triangles: separate quenches performed on the T50 blend. Diamonds: T50′ blend.

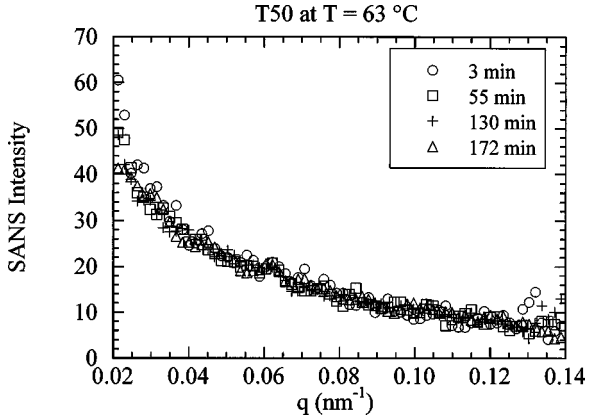

FIG. 22. SANS intensity vs scattering vector at selected times from blend T50 during the 63 °C quench.

teau of I_{inv} will be a strong function of quench depth. This is because the composition of the coexisting phases at equilibrium approach each other as the quench depth is reduced. The differences in I_{inv} obtained at different quench depths thus reflect kinetic differences as well as changes in the equilibrium characteristics. The collapse of d vs t data [Figs. 17(a) and 18(a)] was obtained in spite of the large differences in $I_{\mathrm{inv}}(t)$.

Nucleation experiments are often difficult to reproduce, especially if the nucleation is heterogeneous. We tested reproducibility in our systems by examining samples T50 and T50′. These are two different samples with nearly identical compositions (see Table II). Two temperature quenches to 25 °C were performed on T50 two years after the same quench was conducted on T50′. The source that produces cold neutrons at NIST, where these experiments were carried out, was changed after the T50′ sample was examined. In order to compare the runs before and after the change in the cold source, we divided the T50′ data by a constant (5.0) to empirically account for the changes in the cold source monitor reading. Qualitative agreement between the three data sets was obtained. In Fig. 21, we show the time dependence of the scattering intensity at $q \approx 0.02\ \mathrm{nm}^{-1}$. It is evident from Fig. 21 that the trends in the nucleation data are entirely reproducible in samples with 50% block copolymer. Due to limited access to the neutron beam and the success of these experiments, we did not repeat the other quenches.

As a final check of our experimental protocol, we quenched sample T50 to 63 °C. As indicated in Fig. 5(a), this quench is located slightly above the binodal curve estimated from static measurements, i.e., it is located in the single-phase regime. In Fig. 22 we show the time-resolved scattering results that were obtained during this quench. The experiment was terminated after 3 h, because we observed no evidence of nucleation during this time. All of the other quenches showed significant changes in the SANS profiles after 3 h.

H. Critical length scale during nucleation

We conclude this section by discussing the significance of q_{merge}, the characteristic scattering vector for a given quench beyond which the SANS intensity is independent of time (see Figs. 10–12). It is important to note that q_{merge} was identified in all of the quenches into (and near) the nucleation regime. It is evident that q_{merge} for a given sample depends on quench depth. For example, in sample T40, the value of q_{merge} at 44 °C is distinctly lower than that obtained at 25 °C [compare Figs. 10(a) and 10(b)]. Increasing the quench temperature to 49 and 54 °C results in a further decrease in q_{merge} [Figs. 10(c) and 10(d)]. It is evident that q_{merge} decreases with decreasing quench depth. The T50 quench data (Fig. 11) and the P35 quench data (Fig. 12), show the same qualitative features: the existence of a merge point q_{merge}, which in most cases, decreases with decreasing quench depth.

In an approximate sense, the formation of structures with a length scale of ξ will result in increased scattering at $q \sim 1/\xi$. The fact that the scattered intensity does not increase at q values greater than q_{merge} sets a lower bound on the length scale of the structures formed during phase separation. This lower bound, defined by the symbol $\xi_{\mathrm{crit}} = 1/q_{\mathrm{merge}}$, increases with decreasing quench depth (Figs. 10–12). For example, in the case of T40, ξ_{crit} increases from 8 to 26 nm when the quench temperature is increased from 25 to 54 °C. Classical nucleation theory[1,3,14,18] predicts the existence of a critical nucleus size (R_{crit}), and that only nuclei with sizes greater than the critical nucleus size will grow spontaneously. The merge point provides direct evidence for the existence of such a critical length scale. However, the classical estimate of R_{crit} is based on the assumption that the nuclei have attained equilibrium.[1] In contrast, the nuclei that we have obtained during the early stage of nucleation in samples T40, T50, and P35 are distinctly out of equilibrium.

In Fig. 23, we summarize the critical length scale of the nucleating structures obtained from all of the samples by plotting ξ_{crit} versus quench depth. In order to display the pressure and temperature quenches on the same plot, we use χ, the Flory–Huggins interaction parameter as the abscissa. The conversion from temperature and pressure to χ were

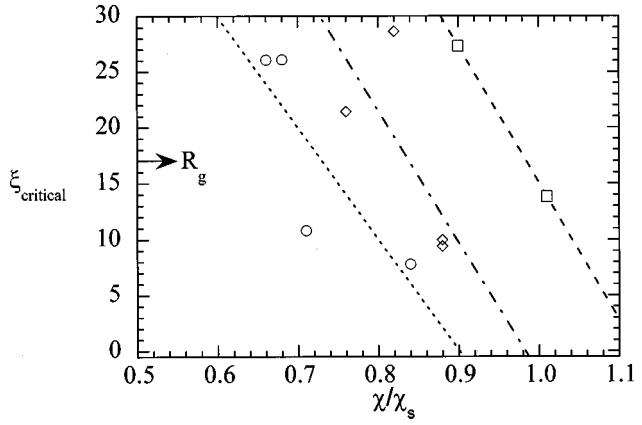

FIG. 23. The critical nucleation length scale, ξ_{crit} vs χ/χ_s for all of the quenches. T40 (circles), T50 (diamonds), P35 (squares). The dashed lines are least squares fits through the data obtained from each sample. The radii of gyration of the polymer chains in our blends (Rg) are in the vicinity of 17 nm.

done using the data in Fig. 1. In addition, we normalized the value of χ with its value at the spinodal, χ_s ($=\chi$ at T_s or P_s). In the case of sample T40, $\chi_s=\chi(T=6\,^\circ\mathrm{C}, P=0\ \mathrm{kbar})=0.002\,38$, while for P35, $\chi_s=\chi(T=32\,^\circ\mathrm{C}, P=0.34\ \mathrm{kbar})=0.001\,73$. The measured values of ξ_{crit} lie between 5 and 30 nm. We thus see that ξ_{crit} can be smaller or larger than the radius of gyration of the polymer molecules ($R_g=17$ nm for all of the components).

IV. CONCLUDING REMARKS

Liquid–liquid phase separation in mixtures of high molecular weight polyolefins was studied by time-resolved neutron scattering. Phase separation was induced by either decreasing temperature or increasing pressure. We focused on data obtained during the initial stages of nucleation, i.e., experiments wherein the sample was quenched to temperatures or pressures that were between the spinodal and the binodal. Separate static neutron scattering experiments were conducted to identify the binodal and spinodal points for each mixture. Phase separation, initiated by both temperature and pressure quenches, yielded similar results. Three regimes were identified during the nucleation process. First, we observe a relatively rapid process wherein concentration fluctuations relax in response to the quench. This is followed by the nucleation regime wherein the neutron scattering intensity increases relatively slowly with time. We call this the early stage of nucleation. The scattering profiles during the early stage are in agreement with the Ornstein–Zernike equation. The structures formed during this stage are indistinguishable from mean-field concentration fluctuations. The exponent of the I vs q scaling in the intermediate q regime, d, was used to determine the fractal dimension of the structures formed during the early stages of phase separation. The value of d obtained during this stage was significantly lower than 3, supporting our conclusion regarding the nature of the structures responsible for nucleation based on the Ornstein–Zernike analysis.

After the early stage of nucleation is completed, phase separation proceeded rapidly. This is indicated by the rapid increase in scattered intensity. The exponent d approaches values between 3 and 4. This is the intermediate stage of phase separation of nucleation and growth, which ultimately leads to the formation of the new liquid phase with sharp interfaces. We demonstrated the existence of time–temperature and time–pressure superposition principle for nucleation. We found that the time dependence of the exponent d for a given blend could be superimposed by a lateral shift of the data along the time axis (log scale). Analogous to the shift factor for viscoelastic behavior of polymers, we define a nucleation shift factor, a_N, which describes the increase in nucleation kinetics with increasing quench depth. The superposition principle applies to data obtained both above and below the classical spinodal, indicating that the crossover from nucleation to spinodal decomposition in our system is smooth and continuous. This was anticipated by Binder and co-workers.[19,20]

For each quench, we find that the scattering intensity is independent of time in the high q regime ($q>q_{\mathrm{merge}}$). This implies the absence of growing structures with length scales smaller than $\xi_{\mathrm{crit}}=1/q_{\mathrm{merge}}$ during nucleation. The length scale ξ_{crit} bears some resemblance to the critical nucleus size predicted by classical nucleation theory.[1]

Aside from the existence of a critical length scale, the nature of the nucleating structures during the early stages is substantially different from the predictions of the classical theories. They are out of equilibrium and qualitatively similar to the diffuse, ramified structures proposed by Binder *et al.*[19,20] and Klein *et al.*[21] Recent experiments and computer simulations indicate that nonequilibrium structures may play an important role in the initial stages of crystal nucleation[58–60] ten Wolde and Frankel studied crystallization of a colloidal suspension from the liquid state by computer simulation.[58] They found that disordered clusters were precursors to nucleation. Likewise, it is has been reported that amorphous density fluctuations are precursors to crystallization of some polymers.[59,60] There is thus increasing evidence that the nuclei formed during the early stages of nucleation in some systems are out of equilibrium.

ACKNOWLEDGMENTS

We thank Jack Douglas for his valuable suggestions, and Chenchy Lin, Ramanan Krishnamoorti and S. V. Jonnalagadda for their contributions during the initial stages of this project. Financial support from the National Science Foundation (CTS-9805852, DMR-9457950), and the Dreyfus Foundation to Polytechnic University is gratefully acknowledged. The SANS instrument at NIST is supported by the National Science Foundation (DMR-9423101).[61]

[1] J. W. Gibbs, *The Scientific Papers of J. Willard Gibbs* (Dover, New York, 1961).
[2] J. W. Cahn, Trans. Am. Inst. Min. Metall. Pet. Eng. **242**, 166 (1968).
[3] J. D. Gunton, M. San Miguel, and P. S. Sahani, in *Phase Transitions* (Academic, New York, 1983), Vol. 8.
[4] J. S. Higgins and H. C. Benoît, *Polymers and Neutron Scattering* (Oxford University Press, Oxford, 1994).
[5] T. Nishi, T. T. Wang, and T. K. Kwei, Macromolecules **8**, 227 (1975).
[6] J. E. Morral and J. W. Cahn, Acta Metall. **19**, 1037 (1971).
[7] T. Hashimoto, M. Itakura, and H. Hasegawa, J. Chem. Phys. **85**, 6118 (1986).

[8] M. Okada and C. C. Han, J. Chem. Phys. **85**, 5317 (1986).
[9] F. S. Bates and P. Wiltzius, J. Chem. Phys. **91**, 3258 (1989).
[10] D. Schwahn, S. Janssen, and T. Springer, J. Chem. Phys. **97**, 8775 (1992).
[11] M. Motowoka, H. Jinnai, T. Hashimoto, Y. Qiu, and C. C. Han, J. Chem. Phys. **99**, 2095 (1993).
[12] H. Jinnai, H. Hasegawa, T. Hashimoto, and C. C. Han, J. Chem. Phys. **99**, 4845 (1993).
[13] H. Jinnai, H. Hasegawa, T. Hashimoto, and C. C. Han, J. Chem. Phys. **99**, 8154 (1993).
[14] P. G. Debenedetti, *Metastable Liquids Concepts and Principles* (Princeton University Press, Princeton, 1996).
[15] W. Zhuang and E. Kiran, Polymer **39**, 2903 (1998).
[16] Y. Xiong and E. Kiran, Rev. Sci. Instrum. **69**, 1463 (1998).
[17] C. C. Lin, H. S. Jeon, N. P. Balsara, and B. Hammouda, J. Chem. Phys. **103**, 1957 (1995).
[18] J. S. Langer and A. J. Schwartz, Phys. Rev. A **21**, 948 (1980).
[19] K. Binder and D. Stauffer, Adv. Phys. **25**, 343 (1976).
[20] K. Binder, Phys. Rev. A **29**, 341 (1984).
[21] A. Sur, J. L. Lebowitz, J. Marro, and M. H. Kalos, Phys. Rev. B **15**, 3014 (1977).
[22] D. W. Heermann and W. Klein, Phys. Rev. B **27**, 1732 (1983).
[23] S. Krishnamurthy and W. I. Goldburg, Phys. Rev. A **22**, 2147 (1980).
[24] A. Cumming, P. Wiltzius, F. S. Bates, and J. H. Rosedale, Phys. Rev. A **45**, 885 (1992).
[25] K. Schatzel and B. J. Ackerson, Phys. Rev. E **48**, 3766 (1993).
[26] P. G. de Gennes, *Scaling Concepts in Polymer Physics* (Cornell University Press, Ithaca, 1979).
[27] C. Herkt-Maetzky and J. Schelten, Phys. Rev. Lett. **51**, 896 (1983).
[28] A. J. Staverman and J. H. Van Saten, Recl. Trav. Chim. Pays-Bas. **60**, 76 (1941).
[29] M. L. Huggins, J. Phys. Chem. **49**, 151 (1942).
[30] P. J. Flory, J. Phys. Chem. **10**, 51 (1942).
[31] A. A. Lefebvre, J. H. Lee, N. P. Balsara, B. Hammouda, R. Krishnamoorti, and S. Kumar, Macromolecules **32**, 5460 (1999).
[32] N. P. Balsara, A. A. Lefebvre, J. H. Lee, C. C. Lin, and B. Hammouda, AIChE. J. **44**, 2515 (1998).
[33] N. P. Balsara, S. V. Jonnalagadda, C. C. Lin, C. C. Han, and R. Krishnamoorti, J. Chem. Phys. **99**, 10011 (1993).
[34] C. C. Lin, S. V. Jonnalagadda, N. P. Balsara, C. C. Han, and R. Krishnamoorti, Macromolecules **29**, 661 (1996).
[35] N. P. Balsara, C. C. Lin, and B. Hammouda, Phys. Rev. Lett. **77**, 3847 (1996).
[36] H. S. Jeon, J. H. Lee, N. P. Balsara, B. Majumdar, L. J. Fetters, and A. Faldi, Macromolecules **30**, 973 (1997).
[37] B. Hammouda, N. P. Balsara, and A. A. Lefebvre, Macromolecules **30**, 5572 (1997).
[38] H. S. Jeon, J. H. Lee, and N. P. Balsara, Phys. Rev. Lett. **79**, 3274 (1997).
[39] J. H. Lee, H. S. Jeon, N. P. Balsara, and M. C. Newstein, J. Chem. Phys. **108**, 5173 (1998).
[40] H. S. Jeon, J. H. Lee, and N. P. Balsara, Macromolecules **31**, 3328 (1998).
[41] H. S. Jeon, J. H. Lee, N. P. Balsara, and M. C. Newstein, Macromolecules **31**, 3340 (1998).
[42] N. P. Balsara, Curr. Opin. Solid State Mater. Sci. **3**, 589 (1998).
[43] H. Rachapudy, G. G. Smith, V. R. Raju, and W. W. Graessley, J. Polym. Sci., Polym. Phys. Ed. **17**, 1211 (1979).
[44] M. Morton and L. J. Fetters, Rubber Chem. Technol. **48**, 359 (1975).
[45] R. Krishnamoorti, W. W. Graessley, N. P. Balsara, and D. J. Lohse, Macromolecules **27**, 3073 (1994).
[46] N. P. Balsara, L. J. Fetters, N. Hadjichristidis, D. J. Lohse, C. C. Han, W. W. Graessley, and R. Krishnamoorti, Macromolecules **25**, 6137 (1992).
[47] D. Schwahn, K. Mortensen, T. Springer, H. Yee-Madeira, and R. Thomas, J. Chem. Phys. **87**, 6078 (1987).
[48] H. E. Cook, Acta Metall. **18**, 297 (1970).
[49] D. Broseta and G. H. Fredrickson, J. Chem. Phys. **93**, 2927 (1990).
[50] M. W. Matsen and M. Schick, Macromolecules **27**, 187 (1994).
[51] R. J. Roe and D. Rigby, Adv. Polym. Sci. **82**, 103 (1987), and references therein.
[52] F. S. Bates, W. W. Maurer, P. M. Lipic, M. A. Hillmyer, K. Almdal, K. Mortensen, G. H. Fredrickson, and T. P. Lodge, Phys. Rev. Lett. **79**, 849 (1997).
[53] K. B. Migler and C. C. Han, Macromolecules **31**, 360 (1998).
[54] The value of τ_F was determined using the two line least-squares fitting procedure that was used to determine T_b. This enabled separation of the data into two sets: the ''short'' time, fluctuation relaxation stage, *F*, and the ''long'' time, early stage, *E*. τ_F is the shortest time in the long time data set. The time defining the end of the early stage, τ_E, could not be determined by the two line least-squares approach because the crossover from the early to the intermediate stage (*E* to *I*) was gradual [e.g., Fig. 13(b)]. To determine τ_E, the slope of the least-squares line through a minimum of four data points was determined, and then another point was added and the slope calculated. These slopes were then averaged. After each subsequent point was added and the slope calculated, the new slope was compared to the average slope. If the slope increased by more than 5% of the average, the time of the previous data point was designated τ_E. Otherwise a new average slope was determined, and the procedure repeated.
[55] Y. Feng, C. C. Han, M. Takenaka, and T. Hashimoto, Polymer **33**, 2729 (1992).
[56] For the nucleation experiments, at $t=\tau_F$, q_H was defined using the following equation: $\Delta I/I=0.25$, where $\Delta I=[I(\text{at the last measurement taken in the experiment})-I(t=\tau_F)]/I(t=\tau_F)$. For the spinodal decomposition experiments instead of using the intensity profile at $t=\tau_F$ in the equation, the intensity profile at the first time data was taken was used (since $\tau_F=0$). As the experiments proceeded, the value of q_H decreased due to the growth of the phase separated structure. The lowest q value before deviations from the power law relationship were observed is designated q_L. For the nucleation experiments, at $t=\tau_F$, q_{merge} is set equal to q_H. For the spinodal decomposition experiments, q_{merge} is set equal to q_H at the first time data is taken.
[57] J. D. Ferry, *Viscoelastic Properties of Polymers* (Wiley, New York, 1980).
[58] P. R. ten Wolde and D. Frenkel, Science **277**, 1975 (1997).
[59] M. Imai, K. Kaji, and T. Kanaya, Macromolecules **27**, 7103 (1994).
[60] N. J. Terrill, P. A. Fairclough, E. Towns-Andrews, B. U. Komanschek, R. J. Young, and A. J. Ryan, Polymer **39**, 2381 (1998).
[61] Certain equipment and instruments or materials are identified in this paper in order to adequately specify the experimental details. Such identification does not imply recommendation by the National Institute of Standards and Technology, nor does it imply the materials are necessarily the best available for the purpose.